Ocean Dynamics (2016) 66:1475–1495
DOI 10.1007/s10236-016-0994-3

A depth-averaged 2-D model of flow and sediment transport in coastal waters

Alejandro Sanchez[1,2] · **Weiming Wu**[3] · **Tanya M. Beck**[2]

Received: 2 March 2016 / Accepted: 8 September 2016 / Published online: 1 October 2016
© Springer-Verlag Berlin Heidelberg 2016

Abstract A depth-averaged 2-D model has been developed to simulate unsteady flow and nonuniform sediment transport in coastal waters. The current motion is computed by solving the phase-averaged 2-D shallow water flow equations reformulated in terms of total-flux velocity, accounting for the effects of wave radiation stresses and general diffusion or mixing induced by current, waves, and wave breaking. The cross-shore boundary conditions are specified by assuming fully developed longshore current and wave setup that are determined using the reduced 1-D momentum equations. A 2-D wave spectral transformation model is used to calculate the wave height, period, direction, and radiation stresses, and a surface wave roller model is adopted to consider the effects of surface roller on the nearshore currents. The nonequilibrium transport of nonuniform total-load sediment is simulated, considering sediment entrainment by current and waves, the lag of sediment transport relative to the flow, and the hiding and exposure effect of nonuniform bed material. The flow and sediment transport equations are solved using an implicit finite volume method on a variety of meshes including nonuniform rectangular, telescoping (quadtree) rectangular, and hybrid triangular/quadrilateral meshes. The flow and wave models are integrated through a carefully designed steering process. The model has been tested in three field cases, showing generally good performance.

Keywords Shallow water flow · Nonuniform sediment transport · Coastal morphodynamics · Two-dimensional · Finite volume method

Responsible Editor: Richard Signell

✉ Weiming Wu
wwu@clarkson.edu

[1] Hydrology Engineering Center, U.S. Army Corps of Engineers, Davis, CA, USA

[2] Coastal and Hydraulics Laboratory, U.S. Army Corps of Engineers Research and Development Center, Vicksburg, MS 39180, USA

[3] Department of Civil and Environmental Engineering, Clarkson University, Potsdam, NY 13699, USA

1 Introduction

The coastal environment is very dynamic in nature due to time-varying forcing by astronomical tide, wind, and waves, as well as complex interactions between currents, waves, and morphology changes. Natural or anthropogenic-induced morphology changes can interfere with or cause damage to coastal structures. Many coastal engineering projects often require to some degree prediction of coastal morphology evolution for planning or design purposes. Modeling of the morphodynamic processes in the coastal zone has been a challenging but crucial task for coastal sedimentation engineering.

Coastal morphodynamic models can be classified into one-dimensional (1D) shoreline evolution models, 1D and vertical two-dimensional beach profile evolution models, two-dimensional horizontal (2DH) area models, and three-dimensional (3D) models. 1D shoreline evolution models describe changes in shoreline horizontal position caused by longshore sediment transport gradients (e.g., Pelnard-Considere 1956; Hanson and Kraus 1989; Szmytkiewicz et al. 2000; van der Salm 2013). Beach profile evolution models compute changes in cross-shore morphology (e.g., Hedegaard and Deigaard 1988; Larson and Kraus 1989; Nairn and Southgate 1993; Bosboom et al. 1997; Johnson et al. 2012). 2DH and 3D morphodynamic models (e.g., Buttolph et al. 2006; Lesser et al. 2004; Lu et al. 2005;

Warner et al. 2008; Sanchez and Wu 2011) compute both longshore and cross-shore morphology changes, using basic principles including the conservation of water and sediment mass and the transport of water momentum and wave energy. These models consider astronomical tidal forcing, atmospheric pressure and wind forcing, wave-current interactions, Coriolis force, bottom and wall friction, and river discharge. 2DH and 3D process-based morphodynamic models capable of simulating short-term (hours to days) and long-term (decades) periods have increasingly become popular in engineering studies due to increased computer speeds and user-friendly interfaces.

Coastal morphodynamic models based on the 3D Reynolds-averaged Navier-Stokes equations for incompressible flow are generally expensive. Therefore, 2DH models have found the most use in practical engineering applications. A limitation of 2DH models is that they do not resolve the vertical current velocity structures which lead to dispersion of momentum and sediments. To overcome this limitation, several 2D hydrodynamic models have been proposed which incorporate the vertical velocity structures and dispersion terms (de Vriend and Stive 1987; Sánchez-Arcilla et al. 1990; Svendsen et al. 2002; Wu 2007). However, a simple but still widely used approach is to extend the eddy viscosity and diffusion coefficient in the momentum and scalar transport equations to mixing or general diffusion which includes the effects of molecular diffusion, turbulent diffusion, and dispersion.

Most coastal sediment transport models are based on the assumption that bed load or total load (both bed and suspended loads) is instantaneously in equilibrium on each computational node (e.g., Struiksma et al. 1985; Chesher et al. 1993; Roelvink and van Banning 1994; Ranasinghe et al. 1999; Cayocca 2001; Fortunato and Olveira 2004; Buttolph et al. 2006; Kubatko et al. 2006; Warner et al. 2008). These models calculate the transport rate using empirical formulas and then determine the bed change by solving the sediment balance equation or the Exner (1925) equation. However, because of the dynamic nature of currents and waves on the coast, the bed load and especially the suspended load are generally not in an equilibrium state. The assumption of local equilibrium may lead to unrealistic results and instabilities that can mask the bed changes and limit long-term simulations (Johnson and Zyserman 2002). A more realistic modeling approach is to solve the nonequilibrium transport equations for bed and suspended loads, which describe the temporal and spatial lags between flow and sediment transport (e.g., Han 1980; Phillips and Sutherland 1989; Wu 2004; Sanchez and Wu 2011). Compared to the equilibrium approach, the nonequilibrium sediment transport modeling is usually more stable and can more easily handle over- and underloading as well as hard (nonerodible) bottoms.

The influence of nonuniform or heterogeneous sediment properties on coastal processes is commonly underestimated due to the difficulty in characterizing and quantifying these types of sediments (Holland and Elmore 2008). Many empirical formulas and numerical models of coastal sediment transport assume uniform or homogeneous sediments. A limited number of studies have addressed nonuniform sediment transport in coastal environments. However, nonuniform sediment transport exists in coastal waters; in particular, sediment sizes vary significantly in coastal inlets than adjacent beaches and bays due to the variability in tidal and wave energy. For most beaches, coarser sediments are generally found in the swash zone and the wave breaker line while finer sediments are found in the trough and landward of the breaker line (e.g., Mason and Folk 1958; Wang et al. 1998). The hiding, exposure, and armoring in the nonuniform bed material may significantly affect sediment transport, morphological change, bed roughness, wave dissipation, etc. It is necessary to develop multiple-sized sediment transport analysis methods and models for coastal sedimentation.

In this study, an implicit depth-averaged 2-D model has been developed to simulate the nonequilibrium transport of nonuniform sediments under actions of currents and waves in coastal waters. The present model is based on the previous versions of the Coastal Modeling System (CMS2D) of the U.S. Army Corps of Engineers (Buttolph et al. 2006; Sanchez and Wu 2011). The previous versions consider single-sized sediment transport and adopt an explicit hydrodynamic solver on a rectangular mesh, which is inconvenient for complex domains and mesh refinement. The present model uses the phase-averaged 2-D shallow water flow equations reformulated in terms of total-flux velocity and multiple-sized total-load sediment transport equations which consider the temporal and spatial lags of flow and sediment transport. It adopts an advanced implicit numerical solution algorithm on a variety of flexible and efficient meshes. It also improves the cross-shore boundary condition, eddy viscosity, and steering between flow, sediment, and wave calculations. The governing equations, boundary conditions, numerical solution algorithms, and model validations of the new model are presented in the following sections.

2 Flow model

2.1 2-D shallow water equations

A schematic of the coordinate system and main variables is provided in Fig. 1. Variables are defined spatially in the Cartesian coordinate system (x, y, z), in which x and y are the horizontal coordinates and z is the vertical coordinate (positive is upwards). The vertical datum is usually the sea level or still

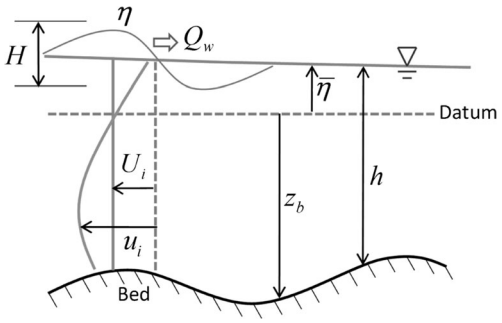

Fig. 1 Sketch of the coordinate system and variables

water level. The bed elevation is denoted as z_b, and the instantaneous and wave-averaged water surface elevations are η and $\overline{\eta}$, respectively. The total water depth is defined as $h = \overline{\eta} - z_b$.

The instantaneous flow velocity, $\hat{u}_i$, is separated into

$$\hat{u}_i = u_i + \tilde{u}_i + u_i^{'} \tag{1}$$

where u_i is the current (wave-averaged) velocity, $\tilde{u}_i$ is the wave (oscillatory) velocity with $\overline{\tilde{u}_i} = 0$ below the wave trough, and $u_i^{'}$ is the turbulent fluctuation. Note that the wave-averaging overbar is omitted for the current velocity u_i for simplicity. The turbulent fluctuation is handled through the Reynolds (or ensemble) averaging, with average $\langle u_i^{'} \rangle = 0$, which has been well documented in literature (Rodi 1993) and thus is not discussed here.

The wave-averaged total volume flux in the water column is

$$hV_i = \overline{\int_{z_b}^{\eta} \hat{u}_i \mathrm{d}z} \tag{2}$$

where V_i is the total flux velocity. The wave- and current-related volume fluxes are given by

$$Q_{wi} = hU_{wi} = \overline{\int_{z_b}^{\eta} \tilde{u}_i \mathrm{d}z} \tag{3}$$

$$hU_i = \overline{\int_{z_b}^{\eta} u_i \mathrm{d}z} = \int_{z_b}^{\overline{\eta}} u_i \mathrm{d}z \tag{4}$$

where U_{wi} is the wave-related phase-averaged flux velocity and U_i is the depth-averaged current velocity. Therefore, the total flux velocity V_i can be written as

$$V_i = U_i + U_{wi} \tag{5}$$

Based on the above definitions and assuming depth-uniform currents (i.e., $u_i(z) = U_i$), the following continuity and momentum equations can be derived by depth-integrating and wave-averaging the 3D Reynolds-averaged Navier-Stokes equations (Phillips 1977; Svendsen 2006):

$$\frac{\partial h}{\partial t} + \frac{\partial (hV_j)}{\partial x_j} = 0 \tag{6}$$

$$\frac{\partial (hV_i)}{\partial t} + \frac{\partial (hV_iV_j)}{\partial x_j} - \varepsilon_{ij} f_c h V_j = -gh\frac{\partial \overline{\eta}}{\partial x_i} - \frac{h}{\rho}\frac{\partial p_a}{\partial x_i} + \frac{\partial}{\partial x_j}\left(\nu_t h \frac{\partial V_i}{\partial x_j}\right) - \frac{1}{\rho}\frac{\partial}{\partial x_j}\left(S_{ij} + R_{ij} - \rho h U_{wi} U_{wj}\right) + \frac{\tau_{Wi}}{\rho} - m_b \frac{\tau_{bi}}{\rho} \tag{7}$$

where t is time; x_i is the horizontal coordinate with subscript $i = 1$ and 2 representing the x- and y-directions, respectively; f_c is the Coriolis force coefficient; $\varepsilon_{ij} = 1$ when $i = 1$ and $j = 2$, $\varepsilon_{ij} = -1$ when $i = 2$ and $j = 1$, and $\varepsilon_{ij} = 0$ otherwise; ρ is the water density; g is the gravitational acceleration; p_a is the atmospheric pressure; ν_t is the eddy viscosity or mixing coefficient; τ_{bi} is the wave-averaged bed shear stress; m_b is a bed slope coefficient; τ_{Wi} is the surface shear stress due to wind forcing determined using the Quadratic law, with drag coefficient given by the formula of Hsu (1988) modified for high wind speeds based on field data by Powell et al. (2003); S_{ij} = wave radiation stress; and R_{ij} = wave roller stress.

Note that the term $hU_{wi}U_{wj}$ in Eq. (7) represents a wave momentum transport and is often ignored or included in the wave radiation stresses. Compared with the hydrodynamic equations derived by Svendsen (2006), Eqs. (6) and (7) use the total flux velocity as the prognostic variable, so that no source-sink term due to waves appears in the continuity equation. In addition, the atmospheric pressure and surface roller terms and bed slope coefficient are considered in Eq. (7) for more general applications. It is also noted that the horizontal mixing term is herein formulated differently as a function of the total flux velocity, similar to the Generalized Lagrangian Mean (GLM) approach (Andrews and McIntyre 1978; Walstra et al. 2000).

The assumption of depth-uniform currents was made to simplify the derivation of Eq. (7). Without this assumption, dispersion terms due to depth-varying currents would appear in Eq. (7) (de Vriend and Stive 1987; Sánchez-Arcilla et al. 1990; Svendsen et al. 2002; Wu 2007). For simplicity, these dispersion terms are combined into the turbulent shear stress terms, so that ν_t includes the molecular viscosity, turbulent viscosity, and dispersion coefficient in general and is thus called the general eddy viscosity or mixing coefficient.

2.2 Bottom friction

Bed shear stress due to current in the case where both current and waves coexist is determined by

$$\tau_{bi} = c_f \rho \left(U^2 + c_w U_{wm}^2\right)^{1/2} U_i \tag{8}$$

where U_{wm} is the maximum orbital bottom velocity of waves, U is the depth-averaged resultant current velocity, $c_f = gn^2/h^{1/3}$, n is Manning's roughness coefficient, and c_w is a coefficient. By averaging the combined instantaneous current and wave velocity squared in a wave period, one can derive that c_w is equal to 0.5 for sine waves. However, we have calibrated the coefficient c_w equal to 1.33 for regular waves and 0.65 for random waves to better agree with the two-parameter data-based method of Soulsby (1997). This difference between the theoretical and calibrated c_w values may be due to the fact that U is the depth-averaged current velocity and U_{wm} is a bottom wave velocity.

In the presence of a sloping bed, the bottom friction acts on a larger surface area for the same horizontal area. This increase in bottom friction is included through the coefficient m_b in Eq. (7), which is given as (Mei 1989; Wu 2007)

$$m_b = \sqrt{(\partial z_b/\partial x)^2 + (\partial z_b/\partial y)^2 + 1} \tag{9}$$

In most morphodynamic models, the bottom slope is small and m_b is neglected. However, it is included here for completeness.

2.3 Eddy viscosity or mixing coefficient

The general eddy viscosity or mixing coefficient may be affected by current, waves, and wave breaking in coastal waters. A simple linear combination of these three components is used in this study:

$$\nu_t = \nu_{t,c} + \nu_{t,w} + \nu_{t,b} \tag{10}$$

where subscripts c, w, and b indicate current, waves, and wave breaking, respectively. The current eddy viscosity $\nu_{t,c}$ can be determined using several turbulence models, including the depth-averaged parabolic eddy viscosity model, the modified subgrid model, and the modified mixing length model. The modified mixing length model is the combination of the depth-averaged parabolic eddy viscosity model and the mixing length model (Wu 2007):

$$\nu_{t,c} = \sqrt{(\alpha_0 U_* h)^2 + \left(l_h^2|\overline{S}|\right)^2} \tag{11}$$

where $|\overline{S}| = \left[2(\partial U_x/\partial x)^2 + 2\left(\partial U_y/\partial y\right)^2 + \left(\partial U_x/\partial y + \partial U_y/\partial x\right)^2\right]^{1/2}$, with U_x and U_y being the depth-averaged current velocities in x- and y-directions; U_* is the bed shear velocity; α_0 is an empirical coefficient, set as $\kappa/6$, with κ being the von Karman constant; and l_h is the horizontal mixing length, determined by $l_h = \kappa \min(c_m h, y)$, with y being the distance to the nearest wall and c_m an empirical coefficient between 0.3 and 1.2.

Equation (11) takes into account the effects of bed shear and horizontal velocity gradients through the first and second terms on its right-hand side, respectively. An alternative formulation of Eq. (11) is to linearly sum $\alpha_0 U_* h$ and $l_h^2|\overline{S}|$. The modified mixing length model performs better than the depth-averaged parabolic eddy viscosity model that accounts for only the bed shear effect. In addition, if the mixing length is replaced with $l_h = c_s(\Delta x \Delta y)^{1/2}$, Eq. (11) represents the modified subgrid model. Here, c_s is a coefficient, and Δx, Δy are the cell sizes in x- and y-directions, respectively.

Waves contribute significantly to lateral mixing, particularly in the surf zone. The general eddy viscosity due to waves is determined using the Kraus and Larson (1991) formula:

$$\nu_{t,w} = c_{wf} U_{wm} H \tag{12}$$

where H is the wave height and c_{wf} is an empirical coefficient. The coefficient c_{wf} is approximately equal to 1.0 and may vary from 0.5 to 2.

Wave breaking also generates a significant amount of turbulent eddies in the surf zone. Its contribution to general eddy viscosity is determined with (Battjes 1975; Camenen and Larson 2007)

$$\nu_{t,b} = c_{br}\left(\frac{D_b}{\rho}\right)^{1/3} h \tag{13}$$

where D_b is the energy dissipation rate due to wave breaking, and c_{br} is an empirical coefficient. c_{br} is approximately equal to 0.08 and may vary from 0.04 to 0.15.

3 Wave model

3.1 Spectral wave-action balance equation

The flow model is coupled with a 2-D spectral wave transformation model, called CMS-Wave (Lin et al. 2008). This wave model was based on the works of Mase (2001) and Mase et al. (2005). It includes physical processes such as wave shoaling, refraction, diffraction, reflection, wave-current interaction, wave breaking, wind wave generation, white capping of waves, and the influence of vegetation and coastal structures. CMS-Wave considers a steady wave field at each time interval based on a quasi-steady approach. It uses the steady-state wave-action balance equation:

$$\frac{\partial(c_x N)}{\partial x} + \frac{\partial(c_y N)}{\partial y} + \frac{\partial(c_\theta N)}{\partial \theta} = \frac{\kappa_m}{2\sigma}\left[\frac{\partial}{\partial y}\left(CC_g\cos^2\theta\frac{\partial N}{\partial y}\right) - \frac{1}{2}CC_g\cos^2\theta\frac{\partial^2 N}{\partial y^2}\right] - \varepsilon_b N + Q \tag{14}$$

where $N = E(x, y, \sigma, \theta, t)/\sigma$; E is the wave energy per unit water surface area per frequency interval; σ is the relative angular frequency; θ is the wave angle relative to the positive x-direction; C and C_g are wave celerity and group celerity, respectively; c_x, c_y, and c_θ are the propagation velocities with respect

to x, y, and θ, respectively; κ_m is an empirical coefficient; ε_b is a parameter for wave breaking energy dissipation; and Q includes source-sink terms of wave energy due to wind forcing, bottom friction loss, nonlinear wave-wave interaction, vegetation resistance, etc.

The first term on the right-hand side of Eq. (14), introduced by Mase (2001), represents the energy dissipation due to the diffraction effect in the alongshore y-direction, which is implicitly perpendicular to wave direction. Mase (2001) and Mase et al. (2005) suggested κ_m has a possible value between 2.0 and 3.0. Note that the diffraction term requires the y coordinate to be approximately the longshore direction. This is a limitation of the wave model.

The first and second terms on the left-hand side of Eq. (14) represent propagation of wave action density in a horizontal x–y plane, and the third term represents depth-induced and current-induced refraction (with propagation velocity c_θ in θ space). The wave propagation speeds are given as

$$\begin{aligned} c_x &= C_g\cos\theta + U_x \\ c_y &= C_g\sin\theta + U_y \end{aligned} \tag{15}$$

$$\begin{aligned} c_\theta = \frac{\sigma}{\sinh 2kh}\left(\sin\theta\frac{\partial h}{\partial x} - \cos\theta\frac{\partial h}{\partial y}\right) \\ + \cos\theta\,\sin\theta\frac{\partial U_x}{\partial x} - \cos^2\theta\frac{\partial U_x}{\partial y} \\ + \sin^2\theta\frac{\partial U_y}{\partial x} - \sin\theta\,\cos\theta\frac{\partial U_y}{\partial y} \end{aligned} \tag{16}$$

where k is the wave number.

The dispersion relations between the relative angular frequency σ, absolute angular frequency ω, wave number vector $\vec{k}$, and current velocity vector $\vec{U}$ are (Jonsson 1990)

$$\sigma = \omega - \vec{k}\cdot\vec{U} \tag{17}$$

$$\sigma^2 = gk\tanh(kh) \tag{18}$$

The depth-limited wave breaking is determined using the criterion of Miche (1951). The spectral energy dissipation is determined by one of the four different formulas: extended Goda formulation (Sakai et al. 1989), extended Miche (Battjes 1972), Battjes and Janssen (1978), and Chawla and Kirby (2002). For the test cases presented here, the Battjes and Janssen (1978) formulation is used. Other parameters of the wave model refer to Lin et al. (2008).

3.2 Surface roller energy equation

As a wave transitions from nonbreaking to fully breaking, part of the energy is converted into momentum which goes into the aerated region of water known as the surface roller. Under the assumption that the surface roller moves in the mean wave direction, the evolution and dissipation of the surface roller energy is calculated by a steady-state energy balance equation (Stive and de Vriend 1994; Ruessink et al. 2001):

$$\frac{\partial(2E_{sr}cw_{mi})}{\partial x_i} = -D_{sr} + f_e D_{br} \tag{19}$$

where E_{sr} is the surface roller energy density, c is the roller propagation speed, $w_{mi} = (\cos\theta_m, \sin\theta_m)$ is the wave unit vector, θ_m is the mean wave direction, D_{sr} is the roller energy dissipation, D_{br} is the wave breaking dissipation (from the wave model), and f_e is the efficiency factor for wave breaking energy transfer to roller.

The roller speed is calculated using the long wave approximation $c = \sqrt{gh}$. The efficiency factor, f_e, is introduced so that only a portion of the wave breaking energy is transferred into the roller. A similar parameter was introduced by Tajima and Madsen (2006). f_e is difficult to estimate but is expected to be a function of the breaker type. Here, it is taken as a calibration parameter with a default value of 1.0.

The roller energy dissipation is approximated as

$$D_{sr} = \frac{2gE_{sr}\beta_D}{c} \tag{20}$$

where β_D is a roller dissipation coefficient approximately equal to 0.05 for regular waves and 0.05–0.1 for general applications.

3.3 Wave radiation and roller stresses

The wave radiation stresses are approximated using the linear wave theory as follows (Phillips 1977; Dean and Dalrymple 1991; Mei 1989; Svendsen 2006):

$$S_{ij} = \iint E(f,\theta)\left[n_g w_i w_j + \delta_{ij}\left(n_g - 0.5\right)\right] \mathrm{d}f\,\mathrm{d}\theta \tag{21}$$

where E is the wave energy density, f is the wave frequency, w_i is the wave unit vector $(\cos\theta, \sin\theta)$, $n_g = 0.5(1 + 2kh/\sinh 2kh)$, and δ_{ij} is the Kronecker delta.

The wave roller stresses are determined by

$$R_{ij} = 2E_{sr}w_{mi}w_{mj}. \tag{22}$$

3.4 Wave flux velocity

In the presence of waves, the oscillatory wave motion produces a net time-averaged mass (volume) transport referred to as Stokes drift. In the surf zone, the surface roller also provides a contribution to the mean wave mass flux. The wave

flux velocity, U_{wi}, is approximated here as (Phillips 1977; Ruessink et al. 2001; Svendsen 2006)

$$U_{wi} = \frac{Q_{wi}}{h} = \frac{(E_w + 2E_{sr})w_{mi}}{\rho hc} \tag{23}$$

where E_w = total wave energy $E_w = \iint E(f,\theta)\mathrm{d}f\,\mathrm{d}\theta$, E_{sr} = surface roller energy density, and c = wave speed.

The first component of the wave flux velocity is the Stokes velocity, while the second component is due to the surface roller and only present in the surf zone. It is noted that because the Stokes velocity is calculated using the linear wave theory, it is expected to over-predict the wave mass transport in the surf zone (Svendsen 2006). For this reason, the surface roller component is often ignored in order to compensate for the overestimation of the Stokes component (e.g., Roelvink et al. 2010).

4 Sediment transport model

4.1 Sediment transport equation

The moving sediment in the water column is traditionally divided into suspended load and bed load. The bed load moves by rolling, sliding, and saltation in a thin layer of a few particle sizes above the bed, whereas the suspended load is transported by the turbulent flow in the water column above the bed-load layer. To reduce the number of differential equations to be solved, the developed model combines the bed load and suspended load as total load (or bed-material load). On the other hand, the nonuniform sediment mixture is divided into a suitable number of size classes. In the case of low sediment concentration, the influence among the size classes of moving sediment is assumed negligible. Thus, the developed model uses the following equation to compute the transport of the k-th size class of total-load sediment:

$$\frac{\partial}{\partial t}\left(\frac{hC_{tk}}{\beta_{tk}}\right) + \frac{\partial(V_i hC_{tk})}{\partial x_i} = \frac{\partial}{\partial x_i}\left[\varepsilon_s h\frac{\partial(r_{sk}C_{tk})}{\partial x_i}\right] + \frac{U_c h}{L_t}(C_{t*k} - C_{tk}) \tag{24}$$

where C_{tk} is the depth-averaged concentration of sediment; subscript k denote the size class; β_{tk} is a correction factor as the ratio of depth-averaged sediment and flow velocities; ε_s is the sediment diffusion coefficient, assumed to be proportional to the eddy viscosity or mixing coefficient as $\varepsilon_s = \nu_t/\sigma_s$, with σ_s being the Schmidt number which is set as 1.0 as default but may vary with cases; r_{sk} is the ratio of suspended load to total load; C_{t*k} is the depth-averaged total-load concentration at the equilibrium state, determined with one of the sediment transport formulas: Watanabe (1987), Soulsby-van Rijn (Soulsby 1997), Lund-CIRP (Camenen and Larson 2007), or van Rijn (2007a, b); U_c is the resultant velocity of current; and L_t is the total-load adaptation length. Note that the subscript i follows the Einstein summation convention, whereas the subscript k does not.

The depth-averaged total-load concentration in Eq. (24) is defined as $C_{tk} = \int_{z_b}^{\eta} u_c c_k \mathrm{d}z / U_c h$, where c_k is the local sediment concentration and u_c is the stream-wise local current speed. With this definition, the sediment transport is simply written as $q_{tk} = U_c h C_{tk}$. The correction factor is defined as $\beta_{tk} = \int_{z_b}^{\eta} u_c c_k \mathrm{d}z / \left(U_c \int_{z_b}^{\eta} c_k \mathrm{d}z\right)$, which accounts for the time lag (hysteresis) between flow and sediment transport. It has a value close to unity for fine sediments, but decreases with increasing grain size. It is evaluated by assuming the logarithmic or power law for the local flow velocity and the Rouse or Lane-Kalinske distribution of suspended load, as described in Wu (2007).

The total-load adaptation coefficient length L_t can be set as a constant often calibrated using measurement data, or determined by

$$L_t = (1 - r_s)L_b + r_s L_s \tag{25}$$

where L_b and L_s are the bed- and suspended-load adaptation lengths, respectively. The bed-load adaptation length is related to the length of dominant bed forms (Wu 2007) and is about $7.3h$. The suspended-load adaptation length is calculated as $L_s = U_c h/(\alpha_s \omega_{fk})$, in which α_s is the suspended-load adaptation coefficient and ω_{fk} is the sediment settling velocity. α_s can be determined using empirical formulas or calibrated using measured data. Further details refer to Sanchez and Wu (2011) and Wu (2007).

The ratio of suspended load to total load, r_{sk}, appears in the diffusion term of Eq. (24) to account for only the diffusion of suspended load. It is determined with C_{k*}/C_{tk*}, in which C_{k*} and C_{tk*} are the suspended-load and total-load equilibrium concentrations, respectively, determined using the van Rijn (1984a, b) sediment transport equations.

4.2 Bed change equation

The bed change due to the kth size class of sediment is determined as

$$\left(1 - p_m'\right)\left(\frac{\partial z_b}{\partial t}\right)_k = \frac{U_c h}{L_t}(C_{tk} - C_{t*k}) + \frac{\partial}{\partial x_i}\left[D_s U_c h(1 - r_{sk})C_{tk}\frac{\partial z_b}{\partial x_i}\right] + \frac{\partial q_{twi}}{\partial x_i} \tag{26}$$

where p_m' is the porosity of bed material, D_s is the coefficient for bed slope effect, and q_{twi} is sediment transport rate due to wave asymmetry and undertow. The second term on the right-hand side of Eq. (26) represents the effect of bed slope on the movement of bed load and in turn the bed change, so that the factor $1 - r_{sk}$ is applied to account for the ratio of bed load over the total load. The coefficient D_s is a function of flow and

sediment characteristics and may vary case by case. Watanabe (1985) used $D_s = 10$ based on a free-body diagram of the grain on a sloping bed. Struiksma et al. (1985) used $D_s = 4$. Later studies, such as Larson et al. (2003) and Karambas (2003), reported good results with $D_s = 2$. Sanchez and Wu (2011) used a value of about 1 to avoid over-smoothing the morphology change. This value is used in the present study.

The last term on the right-hand side of Eq. (26) considers the effects of wave asymmetry and undertow current on sediment transport. Wave asymmetry and undertow current are two important cross-shore processes in the surf zone. The undertow current is near-bed, towards offshore, whereas wave asymmetry usually yields a net onshore sediment transport. The sediment transport rate due to wave asymmetry and undertow is estimated using the formulas of Larson et al. (2015).

4.3 Bed material sorting equation

To account for the variation of bed material gradation in time and space, the bed material is divided into several layers at each computational node. The surface layer is the mixing layer that directly participates in the exchange with the sediment moving with the flow. There are several mixing or active layer models in literature, such as Karim and Kennedy (1982), Spasojevic and Holly (1993), and Wu (2004). Based on mass balance, the following equation for the variation of bed material gradation in the mixing layer can be derived (Wu 2004):

$$\frac{\partial(\delta_m p_{bk})}{\partial t} = \left(\frac{\partial z_b}{\partial t}\right)_k + p^*_{bk}\left(\frac{\partial \delta_m}{\partial t} - \frac{\partial z_b}{\partial t}\right) \tag{27}$$

where p_{bk} is the bed material gradation in the mixing layer; δ_m is the mixing layer thickness; $\partial z_b/\partial t$ is the total bed change rate, $\partial z_b/\partial t = \sum_{k=1}^{N}(\partial z_b/\partial t)_k$; p^*_{bk} is p_{bk} when $\partial\delta_m/\partial t - \partial z_b/\partial t \le 0$, and p^*_{bk} is the bed material gradation at the subsurface layer (below the mixing layer) when $\partial\delta_m/\partial t - \partial z_b/\partial t > 0$. The first term on the right-hand side of Eq. (27) represents the bed change or exchange between the mixing layer and the moving sediment in the water column, and the last term represents the exchange between the mixing layer and the subsurface layer.

The mixing layer thickness is calculated as

$$\delta_1 = \max(2d_{50}, 0.5H_r) \tag{28}$$

where d_{50} is the median diameter of bed material and H_r is the ripple height. H_r is set as the maximum of the current- and wave-related ripple heights determined using Soulsby's (1997) and van Rijn's (1984a, b, 1989) formulas, respectively.

Details for determining the change in the size composition of the subsurface layers refer to Wu (2004) and Sanchez (2013).

4.4 Correction factor for hiding and exposure in bed material

When the bed material is composed of multiple grain sizes, larger grains have a higher chance of being exposed to the flow while smaller particles have a higher chance of being hidden. For the van Rijn (2007a, b), Soulsby-van Rijn (Soulsby 1997), and Watanabe (1987) transport formulas, the hiding and exposure mechanism is considered by using a correction function to modify the critical shear stress or velocity (Wu 2007). For the Lund-CIRP (Camenen and Larson 2007) transport formula, an alternate approach is needed due to the way in which the Shields number and grain size are included in the formulation; thus, the hiding and exposure correction function is directly used to multiply the transport capacity as follows:

$$C_{t*k} = p_{bk} C^*_{tk} \xi_k \tag{29}$$

where C^*_{tk} is the transport capacity of the kth size class of sediment calculated using the Lund-CIRP formula assuming uniform sediment with the same size. The hiding and exposure correction factor is determined as (Wu et al. 2000)

$$\xi_k = \left(\frac{P_{ek}}{P_{hk}}\right)^m \tag{30}$$

where m is an empirical coefficient (set to 1.0 here for the Lund-CIRP formula) and P_{hk}, P_{ek} are the hidden and exposed probabilities of the kth size class in the bed material calculated as

$$P_{hk} = \sum_{j=1}^{N} p_{bj}\frac{d_j}{d_k + d_j} \quad P_{ek} = \sum_{j=1}^{N} p_{bj}\frac{d_k}{d_k + d_j} \tag{31}$$

where d_k is the diameter of the kth grain size class and N is the number of grain size classes.

5 Boundary conditions

For a well-defined problem governed by Eqs. (6) and (7), the flow discharge or velocity is needed at inflow boundaries, while the water level is usually given at outflow boundaries for a subcritical flow or at inflow boundaries for a supercritical flow. In the context of coastal waters, the water surface elevation is usually specified at the seaward boundary, which can be the time series of tide levels recorded at the boundary, generated using the harmonic analysis of tidal constituents, or predicted using a larger-scale regional model.

Along a cross-shore boundary, it is assumed that a well-developed longshore current exists. Thus, the alongshore (y) momentum equation can be reduced from Eq. (7) as follows:

$$\frac{\partial}{\partial x}\left(\rho\nu_t h\frac{\partial V_y}{\partial x}\right)+\tau_{Wy}+\tau_{Sy}-m_b\tau_{by}=0 \tag{32}$$

where τ_{Sy} is the wave-driven stress defined by $\tau_{Si}=-\partial(S_{ij}+R_{ij}-\rho hU_{wi}U_{wj})/\partial x_j$. Equation (32) prescribes V_y, the alongshore component of current velocity, which is used as the boundary condition at the cross-shore boundary. The cross-shore component of the velocity may be copied from internal nodes.

The water level setup due to waves and winds at the cross-shore boundary can be determined by assuming a zero alongshore gradient of water level or using the following equation reduced from the cross-shore (x) momentum equation (7):

$$\rho gh\frac{\partial\overline{\eta}}{\partial x}=\tau_{Wx}+\tau_{Sx}-m_b\tau_{bx} \tag{33}$$

Near rigid wall boundaries, such as beaches and islands, the wall-function approach is employed (Wu 2004, 2007). A threshold flow depth (a small value, such as 0.02 m in field cases) is used to judge drying and wetting. If the flow depth on a node is larger than the threshold value, this node is considered to be wet; otherwise, this node is dry. Because a fully implicit solver is used in the present model, all the wet and dry nodes participate in the solution. Dry nodes are assigned a zero velocity. The wall-function approach is applied on the water edges between dry and wet nodes. This treatment can avoid "overdried" cells. Although mass is locally conserved at each control volume in the finite volume method, there is mass loss due to the fact that water on a wet cell is ignored in the present implicit algorithm when the cell becomes dry, or mass gain due to that water is added to a dry cell when it becomes wet. However, for a real-life tidal inlet case, the magnitude of mass loss or gain is about 0.01 % or less, which is negligible (Wu and Lin 2015).

For sediment transport, the inflow sediment concentration and its size composition are specified at a river boundary. For a cross-shore boundary or tidal flow boundary, the flow is usually two-way, so that a zero gradient of sediment concentration is specified when outflow occurs and the sediment flux is required when inflow occurs. The inflow sediment concentration at the cross-shore or tidal boundary is set as the transport capacity in this study when measured data are not available. The sediment transport model also requires initial bed material composition, which is especially important in the case of erosion.

6 Numerical methods

6.1 Solution of flow equations

The developed flow model uses a variety of meshes, including classical nonuniform rectangular, telescoping (quadtree) rectangular, and hybrid triangular/quadrilateral meshes shown in Fig. 2. The rectangular mesh can have uniform and nonuniform grid spacing. It is simple in terms of numerical discretization and computer coding, but inconvenient to conform to irregular boundaries and refine the mesh locally. The telescoping rectangular mesh can locally refine the mesh around structures or in high-gradient regions by splitting a coarse cell into four child cells and using as many levels of refinement as necessary. This mesh can improve the accuracy of the model with a relatively small increase in the number of cells. The hybrid triangular/quadrilateral mesh is flexible to generate and easy to conform to irregular boundaries. All the cells, including rectangular, triangular, and quadrilateral, in the computational mesh are numbered by means of a one-dimensional array, and tables are used to determine the connectivity of neighboring cells. This allows for the used grids to exist under the same framework and easily excludes inactive (permanently dry) cells from the computational domain.

The flow model uses the non-staggered grid system and stores the primary variables u-, v-velocity, and water level on the same set of cell centers. Equations (6), (7), and (24) are written in the following general transport equation:

$$\underbrace{\frac{\partial}{\partial t}\left(\frac{h\phi}{\beta}\right)}_{\text{Temporal Term}}+\underbrace{\nabla\cdot(h\vec{V}\phi)}_{\text{Advection Term}}=\underbrace{\nabla\cdot\left(\Gamma h\nabla\phi\right)}_{\text{Diffusion Term}}+\underbrace{S}_{\text{Source Term}} \tag{34}$$

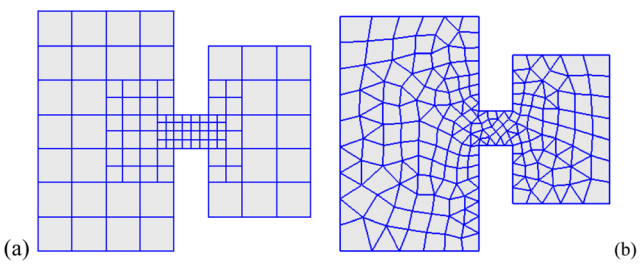

Fig. 2 Computational meshes used for a coastal inlet: **a** telescoping (quadtree) rectangular, **b** hybrid triangular/quadrilateral

where ϕ is the unknown variable representing h, V_i, and C_{tk} for Eqs. (6), (7), and (24), respectively; β is the correction factor, as 1 for Eq. (6) and (7) and β_{tk} for Eq. (24); and Γ is the general diffusion or mixing coefficient.

Integrating Eq. (34) over each control volume and using the Gauss divergence theorem leads to

$$\frac{\partial}{\partial t}\left(\frac{h_P\phi_P}{\beta_P}\right)\Delta A_P + \sum_f h_f\left[V_f\phi_f - \Gamma_f(\nabla_\perp\phi)_f\right]\Delta l_f = S_P\Delta A_P \qquad (35)$$

where ΔA_p is the area of the control volume, subscript P indicates the center of the control volume, subscript f indicates the f-th face of the control volume, Δl_f is the length of face f, and $(\nabla_\perp\phi)_f$ is the outward normal gradient of ϕ at cell face f.

The temporal derivative term in Eq. (35) is discretized using the backward Euler scheme or three-time-level difference scheme, so that implicit solution algorithms with first- and second-order accuracy in time are developed. The convective flux is discretized using one of the hybrid upwind/central difference, exponential difference, and HLPA (Hybrid Linear/Parabolic Approximation; Zhu 1991) schemes. The HLPA scheme has second-order accuracy in space, while the other two have the accuracy between first and second orders. The diffusion flux is determined using the central difference scheme. The final algebraic equations can be derived by arranging into a compact form in which the values of ϕ at cell centers at time level $n + 1$ are unknown. The discretized algebraic equations have sparse, asymmetric matrices of coefficients and are solved iteratively using the flexible GMRES method with ILUT preconditioning.

For solving the continuity and momentum Eqs. (6) and (7) together, the coupling of water level and velocity is achieved by using the SIMPLEC algorithm (van Doormal and Raithby 1984) with under-relaxation. Fluxes at cell faces are determined using Rhie and Chow's (1983) momentum interpolation method to avoid spurious checkerboard oscillations that possibly existed on a non-staggered grid. These numerical methods based on a structured quadrilateral mesh were described in detail by Wu (2004, 2007), extended to the telescoping rectangular mesh by Wu et al. (2011), and then to a hybrid triangular/quadrilateral mesh by Sanchez (2013). The details are not introduced here due to the limit of paper length.

6.2 Solution of sediment equations

The sediment transport model solves the convection-diffusion equation (24) using the same implicit finite volume method on the same meshes as used by the flow model. The bed change equation (26) and bed material sorting equation (27) are discretized using difference schemes in time at each computational node. The near-bed exchange and bed-slope effect terms in Eq. (26) are treated implicitly and explicitly, respectively. The bed material gradation p_{bk} in Eq. (29) is treated implicitly, and Eqs. (24), (26), (27), and (29) are solved together in coupled form that is similar to that described by Wu (2004). This coupled sediment calculation algorithm is efficient and stable.

However, the flow and sediment transport calculations are still decoupled. This means that the flow is calculated by ignoring the effects of sediment transport and bed change on the flow and using the bed topography of the previous time step, and then the sediment transport, bed change, and bed material sorting equations are solved using the calculated flow parameters. This decoupling is usually applicable when the sediment concentration is low and the bed changes slowly.

6.3 Solution of wave equations

The wave model and surface roller model use a rectangular mesh with nonuniform grid spacing in x- and y-directions. The wave mesh can be different from the flow

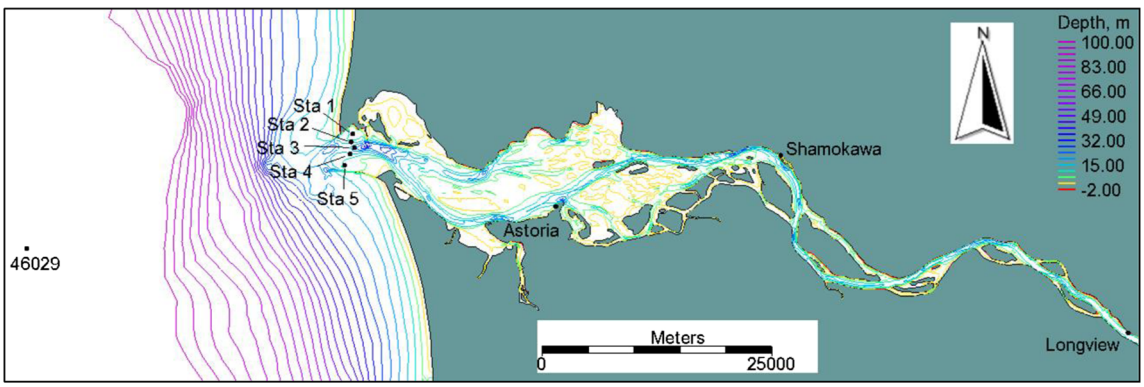

Fig. 3 Map of the Columbia River Estuary. The locations of observation stations are shown with *black dots*. Depth contours beyond 100 m are not shown for better visualization

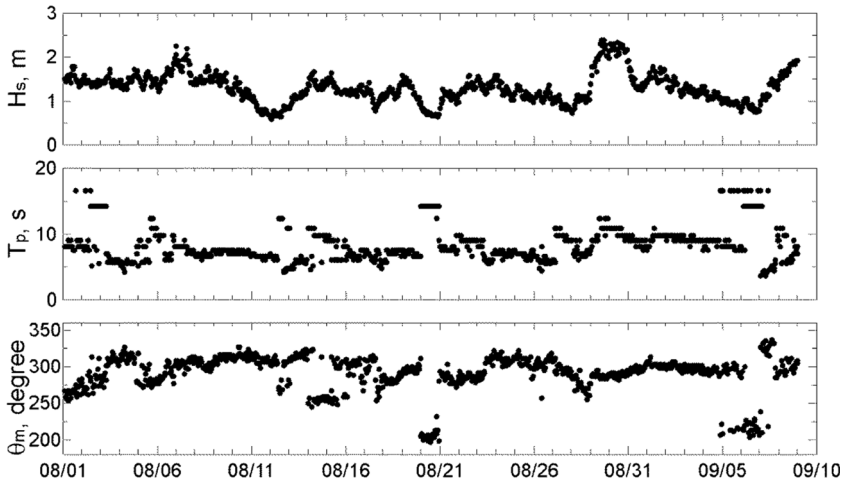

Fig. 4 Wave data from NOAA buoy 46029: H_s = significant wave height, T_p = peak wave period, and θ_m = mean wave direction

model mesh. The wave model solves the wave-action balance equation using a forward marching finite difference method (Mase et al. 2005; Lin et al. 2008). The convection term in the surface roller equation (19) is discretized with the first- or second-order upwind scheme and the discretized equation is solved iteratively using a pseudo-time marching scheme (Sanchez 2013). Because the wave models use a quasi-steady approach, waves were calculated at a large time interval (called steering interval), which may be 0.5–3.0 h.

6.4 Steering of flow and wave models

The flow and wave models are integrated using a process called steering. The wave steering interval can be much larger than the flow time step, so that a wave steering interval is equivalent to multiple flow time steps. Because the flow and wave models are contained in a single code, the steering is conducted in the following steps:

1. The wave model is run for the starting time and the first wave time interval. If turned on, the surface roller model is run on the wave mesh and the roller contribution is added to the wave radiation stress.
2. The wave height, period, direction, dissipation rate, and radiation stress are interpolated spatially from the wave mesh to the flow mesh.
3. The flow model (and sediment transport model if turned on) is run using the wave variables linearly interpolated throughout time during the steering interval. At each flow time step, variables such as wave length and bottom orbital velocity are updated using the new water depth and current velocity.
4. Water level, current velocity, and bed elevation are estimated for the next wave steering interval and interpolated from the flow mesh to the wave mesh.
5. The wave model and surface roller model (if turned on) are then run for the new wave steering interval using the estimated flow properties.
6. Steps 2–5 are repeated until the end of the simulation.

When using a large steering interval, it is important to consider how to pass the water level, current velocity, and bed elevation from the flow to the wave model. For most open coast applications, nearshore waves are most sensitive to variations in water level. In this study, the water level at the wave model time interval is decomposed into spatially constant and variable components. The spatially constant component is assumed to be equal to the tidal level specified at the ocean boundary for the present wave steering interval, and the spatially variable component which includes wind and wave setup is estimated based on results at the previous flow time step. This approach has been found to be sufficient for most applications and is simple to implement.

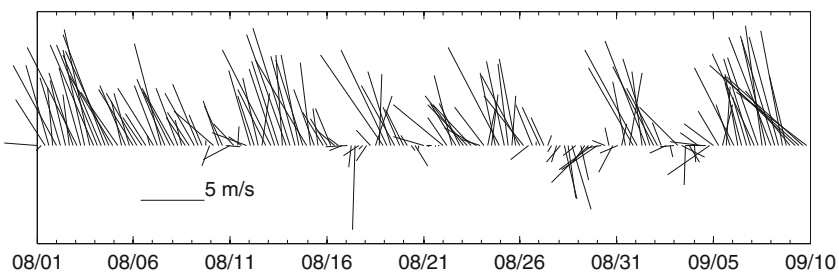

Fig. 5 Wind data from NOAA buoy 46029

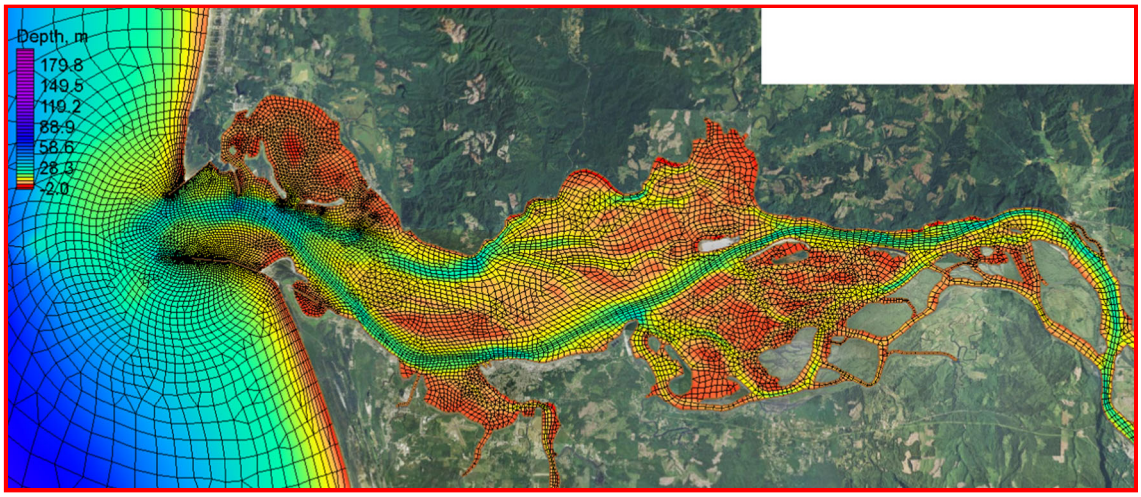

Fig. 6 Flow model mesh near the Columbia River Estuary (deep ocean and upstream channel regions are not shown)

7 Model testing

The developed model has been extensively tested. Three cases are reported here to demonstrate the performance of the developed model in the real-life cases of tidal flow with wave effects in an estuary, morphological evolution of a beach adjacent to a tidal inlet, and channel infilling at a tidal inlet. The simulation results in these test cases are described below.

Case 1: tidal flow in Columbia River Estuary, USA

The Columbia River Estuary is located in the northwestern United States. Its drainage area is 671,000 km^2. The inlet entrance is about 14.5 km wide, with three rubble-mound structures supporting the navigation channel. The tide is mixed semi-diurnal with a mean tidal range of approximately 2.4 m. The Columbia River discharge may vary from 2000 to 4000 m^3/s in the fall to early spring and reaches a maximum of approximately 11,000 m^3/s in the spring/summer due to snow melt (Bottom et al. 2005). During August 3 and September 9 of 2005, the U.S. Army Corps of Engineers (USACE) conducted a field study at the estuary mouth (Moritz 2005). Five bottom-mounted tripods were deployed at the estuary entrance (Fig. 3) to measure currents and waves. Deepwater waves and wind were obtained from the National Oceanic and Atmospheric Administration (NOAA) buoy 46029 location 37 km offshore at the 128-m bathymetric contour. The wave conditions during the study period were relatively moderate with the highest offshore significant wave heights of approximately 2.4 m (Fig. 4). The peak wave periods were typically 8 s but varied between 6 and 16 s. The mean wave direction was predominantly from the Northwest. Wind was generally relatively mild (<10 m/s) and from the north-north-west with short reversals (Fig. 5).

The flow model used a hybrid triangular and quadrilateral mesh of approximately 16,000 cells covering from deep ocean water to the upstream channels at Longview. Figure 6 shows a close view of the mesh near the estuary. The quadrilateral cells were especially useful in representing the navigation channel and river portion of the domain. The grid resolution was approximately 20 m near the jetties and expanded out to approximately 3500 m at the open ocean. The flow

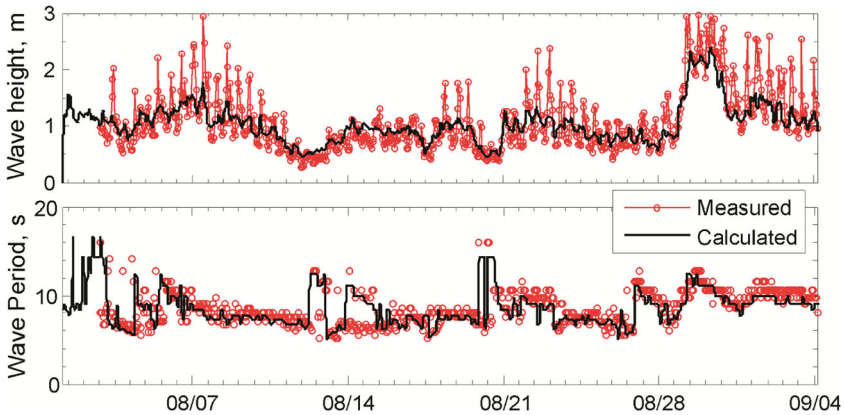

Fig. 7 Measured versus calculated significant wave heights and peak wave periods at Station 5

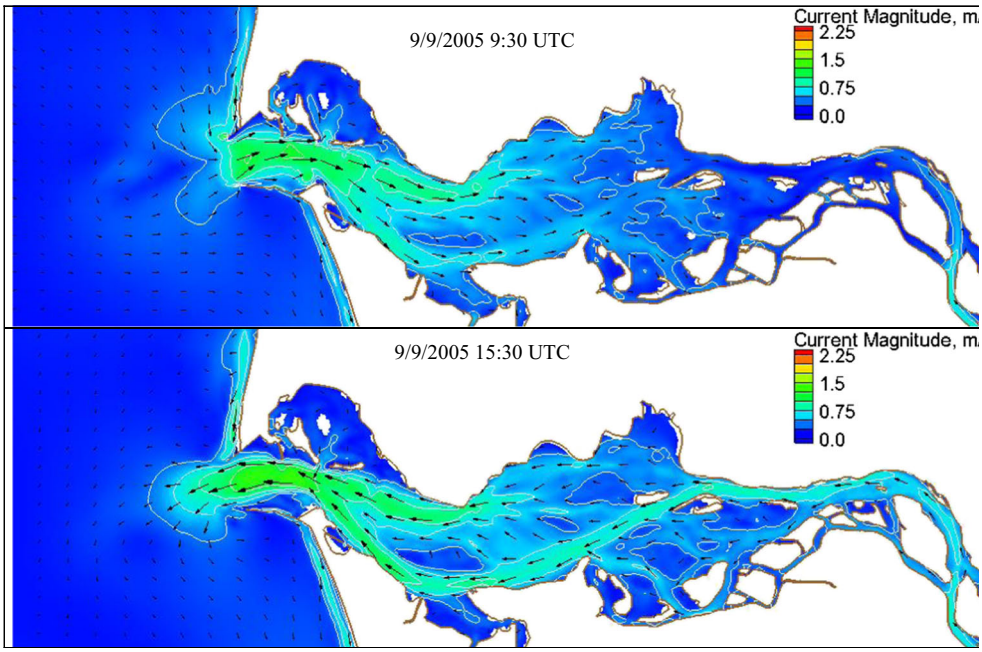

Fig. 8 Example peak flood (*top*) and ebb (*bottom*) currents computed for the Columbia River Estuary

model used a time step of 5 min. The offshore boundary was forced with the tidal constituents obtained by Elias et al. (2012). The daily average river discharge was approximately constant during the study time period, set at

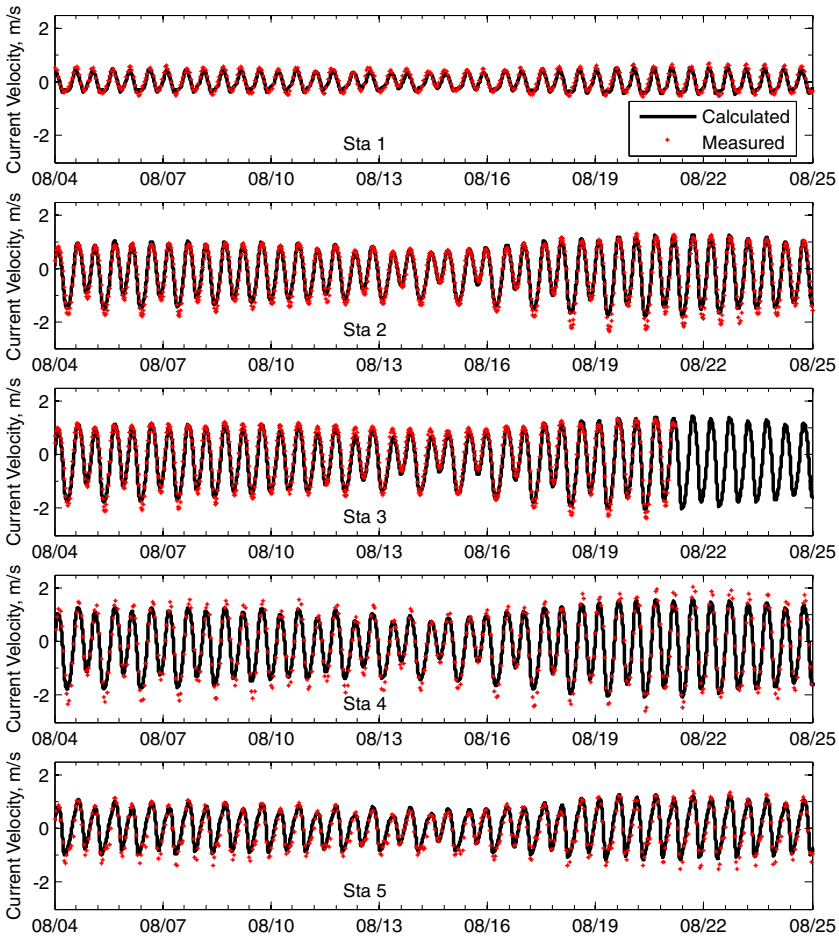

Fig. 9 Comparison of measured and calculated depth-averaged current velocities (principle component) at Stations 1 through 5

4000 m^3/s. Manning's n calibrated using measured water levels increased from 0.018 $s/m^{1/3}$ at the entrance, 0.025 $s/m^{1/3}$ near Astoria, 0.03 $s/m^{1/3}$ near Shamakowa, and to 0.038 $s/m^{1/3}$ near Longview. These values are similar to those reported by Elias et al. (2012).

The wave model used a rectangular mesh of approximately 59,000 cells and with a variable grid resolution between 50 and 600 m. The wave model only covered the area near the entrance. The wave model steering interval was set to 1 h.

The computed significant wave heights and peak wave periods at Station (Sta) 5 are compared with measurements in Fig. 7. The normalized root mean squared error was 11.4 % for significant wave height and 17.9 % for peak wave period. Here, the errors were normalized by the ranges of the corresponding measured quantities. The computed peak wave periods agreed generally well with the measurements. The model reproduced the general variations of wave height but tended to underestimate the wave heights during ebb tides. When the waves encounter the opposing ebb currents, the wavelength is reduced, so that the wave is compressed and the wave height increases. Further research is needed to improve the wave model prediction in this circumstance.

Example snap shots of the peak ebb and flood velocities are shown in Fig. 8. One can see the model can simulate the tidal currents in the estuary, as well as the longshore currents along the coastal lines. A comparison of the measured and computed depth-averaged (principal component) current velocities is presented in Fig. 9. Positive velocities indicate flood and negative velocities indicate ebb. The normalized root mean squared error was less than 9.5 %, and the correlation coefficient R^2 was larger than 0.91 for the five stations. The current velocities were generally better simulated in the central part of the entrance at Stations 2, 3, and 4. The flood velocities were generally well captured except for Station 4, which were slightly under-predicted, while the peak ebb velocities were somewhat underestimated except for Station 1, especially during spring tides. The under-prediction of ebb currents might be due to a constant river flow discharge used and the density current and stratification ignored in the present depth-averaged 2-D model.

The measured and computed water levels at four stations are compared in Fig. 10. The tidal amplitude decreased with

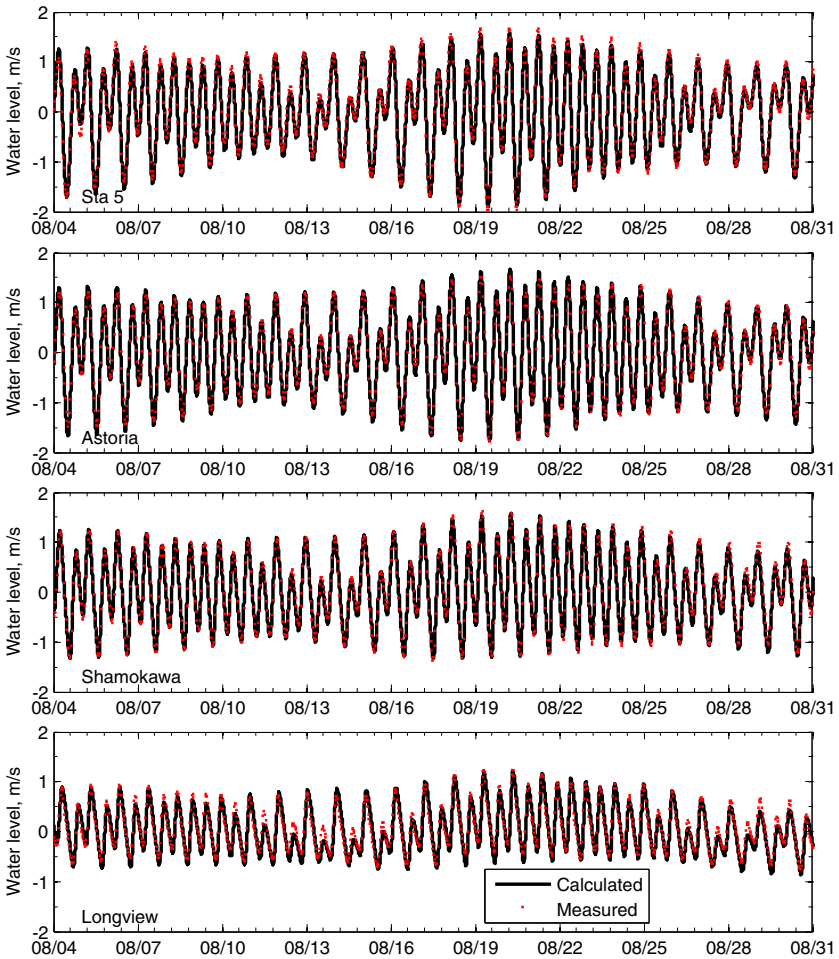

Fig. 10 Comparison of measured and calculated water levels at four tide gauge stations

distance from the entrance due to bottom friction. The water levels were well simulated at all four stations, but the model performance decreased at Longview. The normalized root mean squared error was less than 4.5 % and R^2 is 0.97 for Station 5, Astoria, and Shamakowa, whereas the corresponding statistics were 9.6 % and 0.76 at Longview.

In addition, sensitivity tests were conducted using half the flow grid size; time steps of 5, 10, and 20 min; a larger wave mesh with the same offshore coverage as the flow model; and a steering interval of 30 min. The simulation results are not significantly different and thus are not reported here.

Case 2: beach morphology changes near Grays Harbor Inlet, USA

Grays Harbor Inlet is located on the southwest Washington coast of the northwestern U.S. The estuary has a wetted surface area of approximately 91 mi^2 at mean higher high water and 28 mi^2 at mean lower low water. The main input of fresh water is from the Chehalis River. The 3-mi-wide entrance has two convergent rock jetties which extend from spit points, as shown in Fig. 11. The developed hydrodynamic model was tested by Wu et al. (2011) using the water level, current, and wave data collected in September 1999. In the present study, the model was applied to the beaches adjacent to the inlet to test the model skill in predicting nearshore morphology change using the data observed in May–July 2001.

Between May and July of 2001, the U.S. Geological Survey collected weekly topographic maps and monthly bathymetric surveys along 14 transects spaced 50–200 m apart (Landerman et al. 2004) on the north beach. In addition, grab samples of surface sediment were collected at several locations. Figure 11 shows the locations of the observation stations and nearshore bathymetric profiles. The first half of the field deployment in May 6–30 of 2001 was simulated here. A ramp of 5 days was added to initialize the simulation so that the start date was May 1, 2001. The simulation period was characterized by relatively calm conditions, with a few spring storms with significant wave heights in the order of 3 m. The wave model was run on a ~200,000-cell rectangular grid with varying grid resolution from 15 to 120 m. The waves were forced with spectral wave information from the Coastal Data Information Program (CDIP) buoy No. 03601 located southwest of the inlet at a depth of 42 m. The flow model used a telescoping rectangular grid shown in Fig. 12, which has ~55,000 cells and six levels of refinement from 640 to 20 m. The flow model was forced with a water level time series from Westport Harbor with a negative 30-min phase lag correction, which was obtained by comparing with the stations deployed during the field study (see Fig. 11). Winds were interpolated

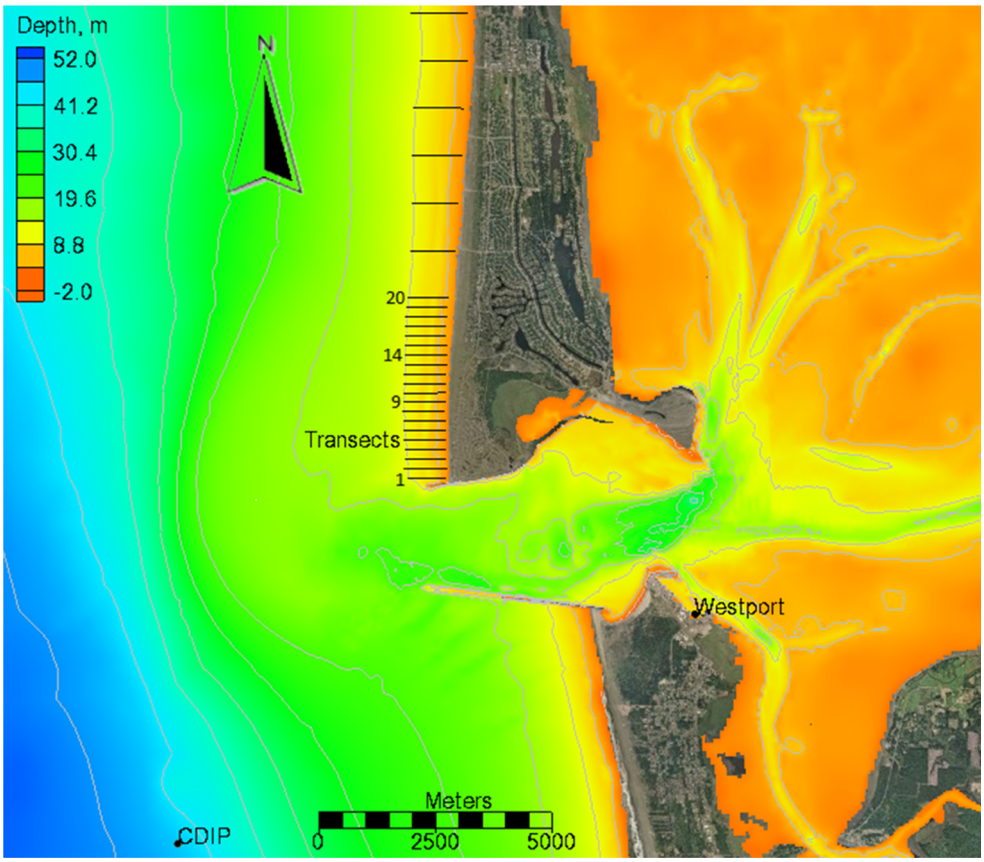

Fig. 11 Map of Grays Harbor inlet, WA showing the location of the nearshore bathymetric transects

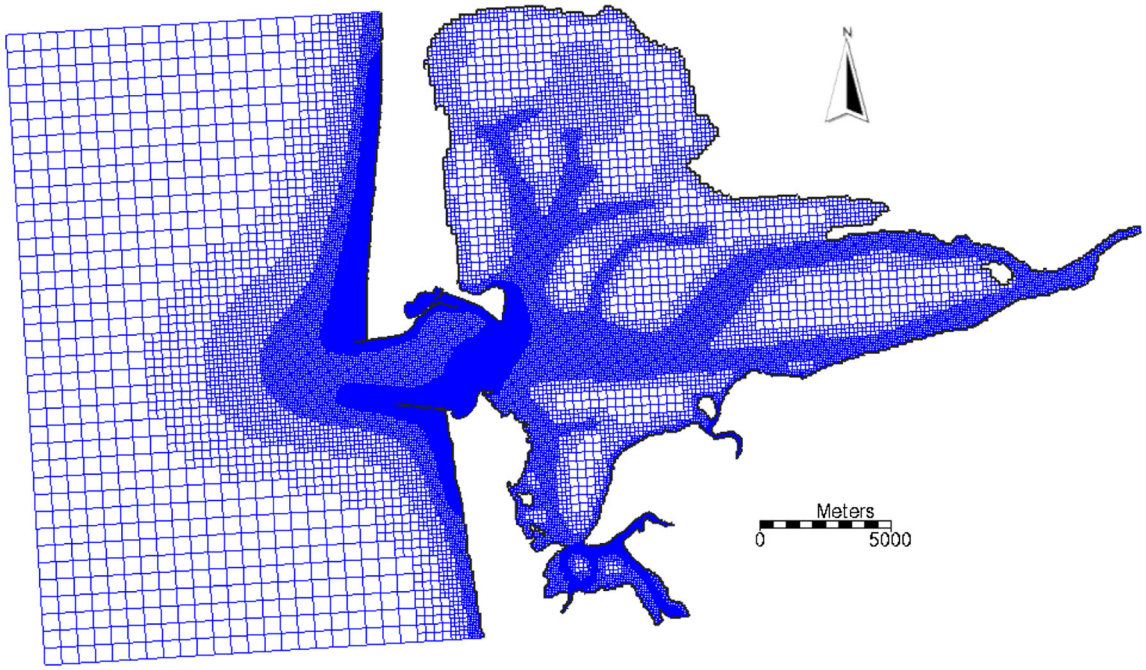

Fig. 12 Flow grid for the Grays Harbor case

from the Blended Sea Winds product of the National Climatic Data Center (Zhang et al. 2006). Manning's coefficient was calibrated in Wu et al. (2011) as 0.018 s/m$^{1/3}$ over the domain, except on the rock structures where a value of 0.1 s/m$^{1/3}$ was used. A flux boundary condition was applied at the Chehalis River, which was obtained from the USGS. The time step for flow and sediment calculations was 10 min. Waves were calculated at a constant 2-h steering interval.

The initial bed material composition was specified by a spatially variable median grain size d_{50} and constant geometric standard deviation σ_g of 1.3 based on field measurements. The initial fractional composition at each cell was assumed to be constant in depth and have a log-normal distribution, and divided to six size classes with representative diameters of 0.1, 0.126, 0.16, 0.2, 0.25, and 0.31 mm. Ten bed layers were used with an initial thickness of 0.5 m each. A constant bed porosity of 0.3 was used in the simulation. The Lund-CIRP transport formula (Camenen and Larson 2007) was used to estimate the transport capacity. The total-load adaptation length L_t was determined using Eq. (25), with the bed-load adaptation length L_b being set to 10 m and the suspended-load adaptation coefficient α_s set to 0.5. The effects of wave asymmetry and undertow current on the sediment transport in the surf zone were considered using the approach suggested by Larson et al. (2015).

A comparison of the measured and computed bed changes on the beach segment of the first four to five transects between May 6 and 30 of 2001 is shown in Fig. 13. Selected regions of interest are encompassed by black lines in order to help visually compare the bed changes. In general, the measured and calculated results show many common features and similar erosion and deposition patterns. More specifically, the bed

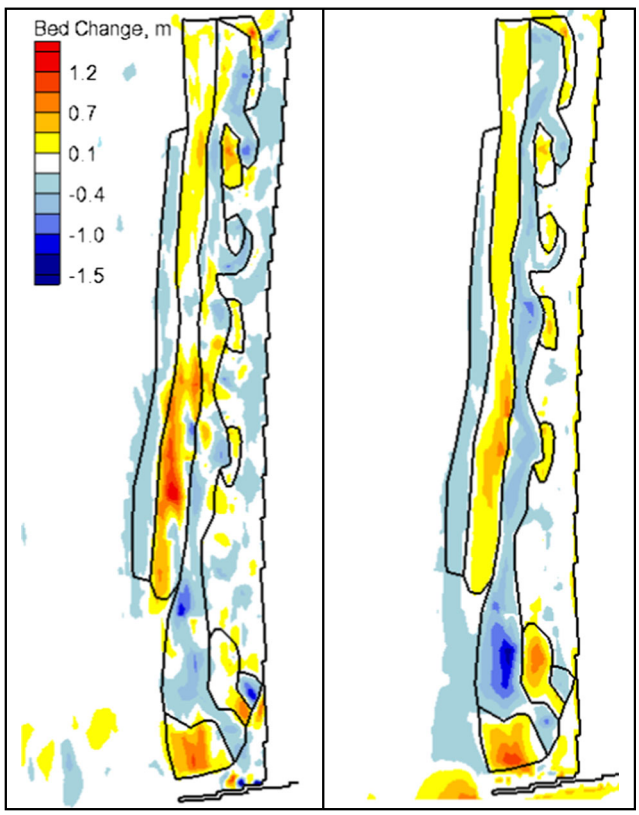

Fig. 13 Measured (*left*) and computed (*right*) bed changes during May 6 and 30, 2001

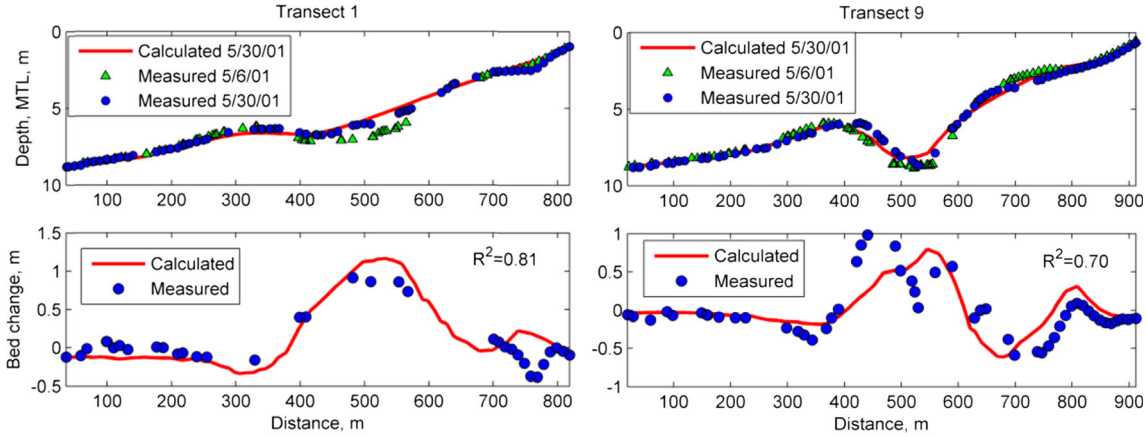

Fig. 14 Measured and computed water depths (*top*) and bed changes (*bottom*) for Transects 1 and 9

change was characterized by erosion of the outer bar, deposition at the outer trough and inner bar face, and erosion of the inner trough face. There was a region extending approximately 1 km from the northern jetty, where the bed changes were noticeably different from those further to the north. This region was interpreted as being strongly influenced by the presence of the inlet, ebb shoal, and northern jetty. Interestingly, both the measurements and model results show that small (200–300 m in length) inner bars formed adjacent to the trough, which appeared at regular 400–500-m intervals. The computed bed changes in the foreshore region (beach face) were relatively small compared to the measurements due to the lack of swash zone processes in the present version of the model.

The measured and computed water depths and bed changes for Transects 1 and 9 are shown in Fig. 14. Most of the bed changes occurred from the nearshore bar to the outer beach face. The model was able to accurately predict an onshore bar migration, although it underestimated the nearshore bar height. R^2 was 0.81 and 0.70 for the bed change predictions in Transects 1 and 9, respectively, and the average R^2 was 0.6 for the 14 transects.

Case 3: channel infilling at Shark River Inlet, USA

The Shark River Inlet is the northernmost inlet on the New Jersey coast of the northeast U.S. The inlet has two parallel rubble stone jetties. The computational domain covered a local scale of approximately 11 km centrally located around

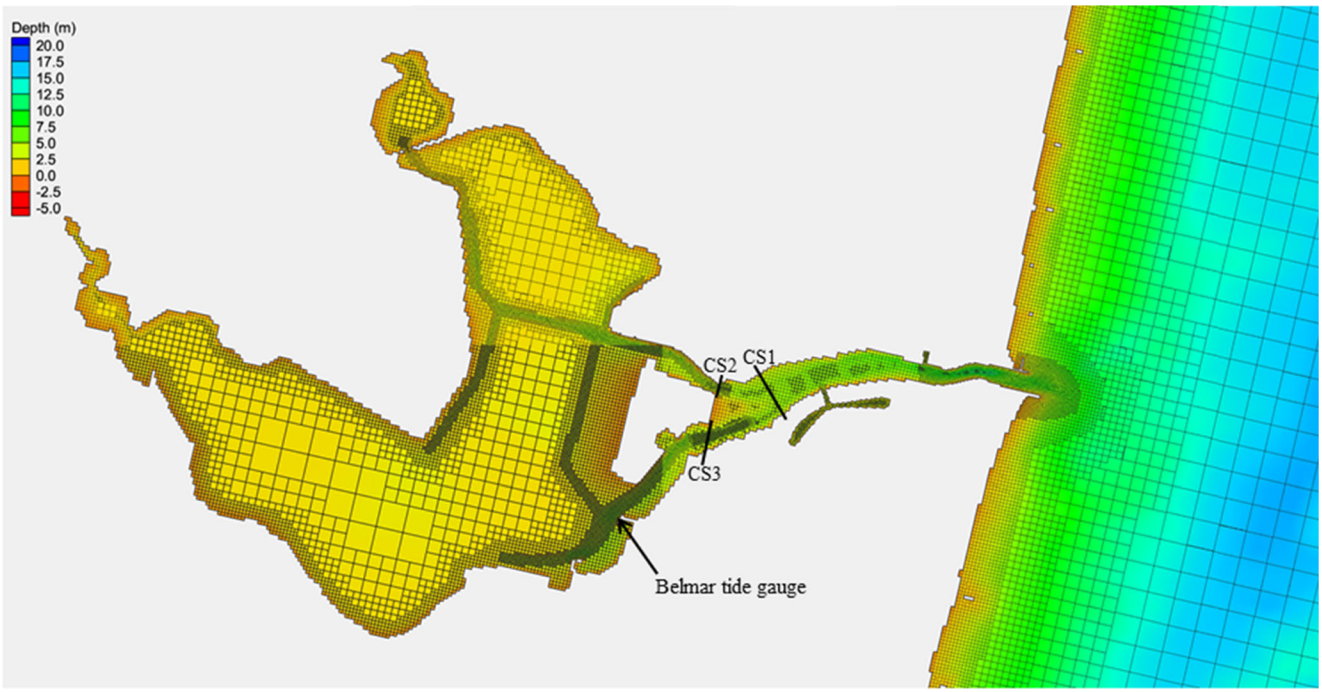

Fig. 15 Flow model mesh for the Shark River Inlet case (deep water region is not shown)

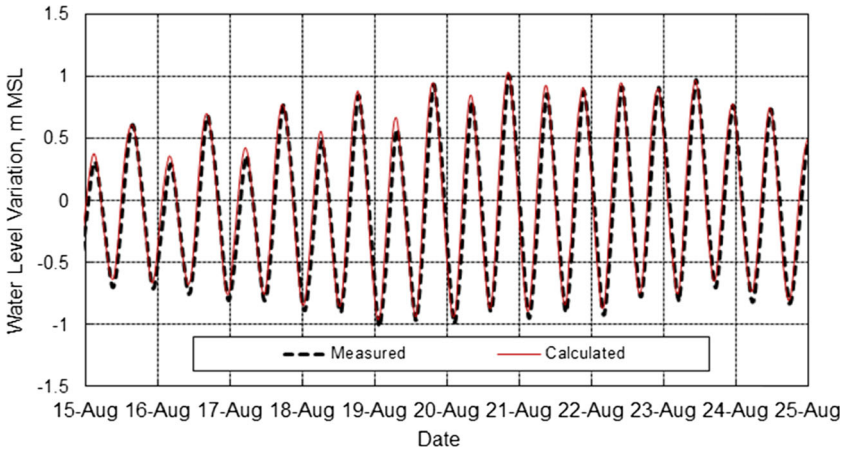

Fig. 16 Measured and calculated water levels at Belmar

Shark River Inlet. Two separate grids were used for the flow and wave models covering the same alongshore distance with the ocean extending seaward 8.5 km for the wave model and 3.5 km for the flow model. The grids were oriented parallel to the shoreline. The flow mesh (Fig. 15) consisted of approximately 20,000 rectangular cells and used five levels of local refinement, with an 8-m cell resolution in the main throat of the inlet and 16-m cell resolution around the jetties and beach, extending out to a 128-m cell size in the ocean. The wave mesh was a nonuniform rectangular grid of 29,256 cells with a minimum cell spacing of 10 m within the inlet entrance channel expanding to 191 m along the outer ocean cells.

The flow model was first tested through a simulation for a 10-day period from August 15 to 25, 2009, without considering sediment transport. The flow model was driven with measured open ocean tide level from a tidal gage at Sandy Hook, NJ, approximately 30 km north of Shark River Inlet. Manning's coefficient was set to 0.02 $s/m^{1/3}$ in the surf zone, 0.025 $s/m^{1/3}$ in the channels, but increased to 0.06 $s/m^{1/3}$ near two bridge crossings to account for the flow drag by bridge pilings. The flow model time step was 15 min. Figure 16 compares the measured and calculated water levels at Belmar tide gauge station within the Shark River Estuary (Fig. 15), showing good agreement in magnitude and phase. Figure 17 compares the calculated and measured current speeds at channel thalwegs of three cross-sections (CS1, 2, and 3 in Fig. 15) within the throat of Shark River Inlet during a complete tidal cycle on August 20, 2009. The normalized mean absolute error is 3–5 % for the currents in the main channel (CS1) and south channel (CS3) and 9 % for the north channel (CS2).

Then, the developed model was tested by using measurements of channel profiles and total infilling volume at the Shark River Inlet entrance channel over a 4-month period from January to April 2009. An existing condition from a January 2009 bathymetry formed the basis to generate a grid for a contemporary representation of the inlet after dredging. The ocean tide level data were still from the tidal gage at Sandy Hook. Because measured wave data were not available for the area, wave data from Wave Information Study (WIS;

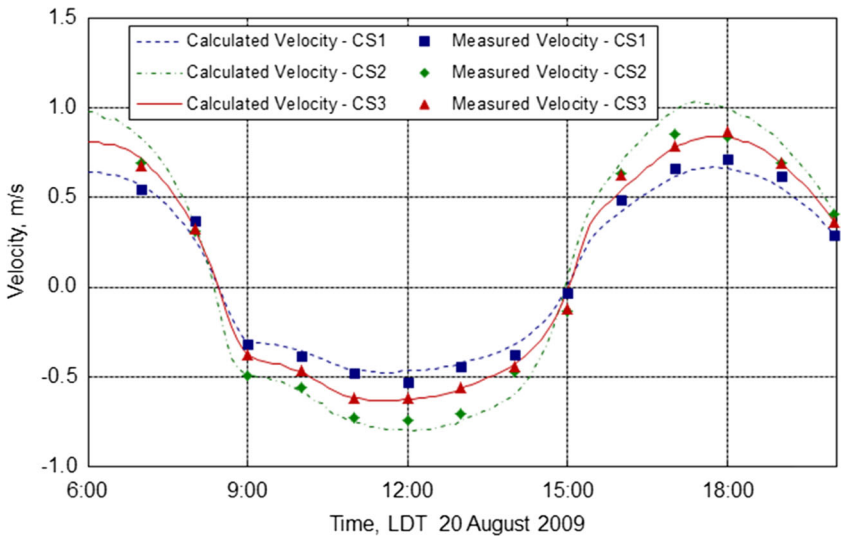

Fig. 17 Calculated and measured currents at channel thalwegs of cross-sections 1, 2, and 3 over a tidal cycle in August 20, 2009

https:\\wis.usace.army.mil/) station 129, approximately 8.5 km off the coast of the study area, provided input parameters for generating spectral waves for the wave model. After analyzing the 20-year wave hindcast, the year 1990 was chosen to force the model as it represents an average wave condition for the January to April time period. The wave grid boundary was located at 26 m, the water depth of the hindcast station. The time step for flow, sediment transport, and bed change was 15 min, and the wave model steering was 3 h.

Five size classes were used to represent the various grain sizes being transported and in the bed. The initial bed composition was defined by assuming an initial log-normal grain size distribution and specifying an initial geometric standard deviation σ_g = 1.8 mm and median grain size d_{50} = 0.26 mm. Using the multiple-sized sediment transport model reduced scour within the channel thalweg and accurately represented the spatial distribution of sediment observed in this region. In addition, the bed material porosity was set as 0.3. Though total-load adaptation lengths of 1, 2, 3, 4, 5, 10, and 100 m were tested, the value 100 m was selected for the final calculations because it produced the most realistic patterns and volumetric changes compared to measurements.

The Lund-CIRP formula was used in for sediment transport capacity, but the formula was multiplied with a scaling factor of 2.0 to match the channel infilling estimates. The scaling factor value of 2 is within the generally accepted range of 0.5–2.0 for empirically derived sediment transport formulas. Based on the surveys, channel infilling volume expected for the 4-month simulation is 8900 m^3 for the entrance channel alone (Fig. 18). The 4-month simulation produced a similar channel infilling volume of 9200 m^3 (with a relative error of 3.3 %).

The measured and calculated entrance channel depths along five transections shown in Fig. 18 are compared in Fig. 19. The measured and calculated morphology changes at the entrance channel were in good agreement. Transects 1 and 2 represented the along-channel sedimentation patterns in the direction of currents. Transect 3 was located within the

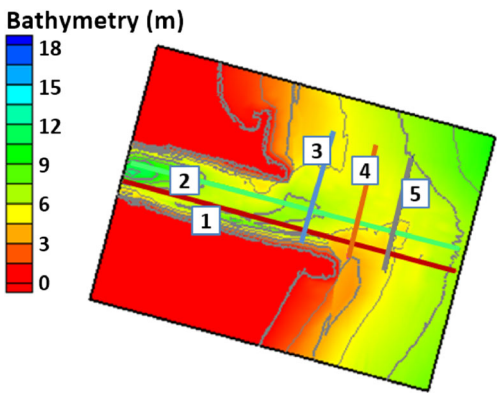

Fig. 18 Locations of transects at the channel of Shark River Inlet (bathymetry contours indicate initial water depths in meters)

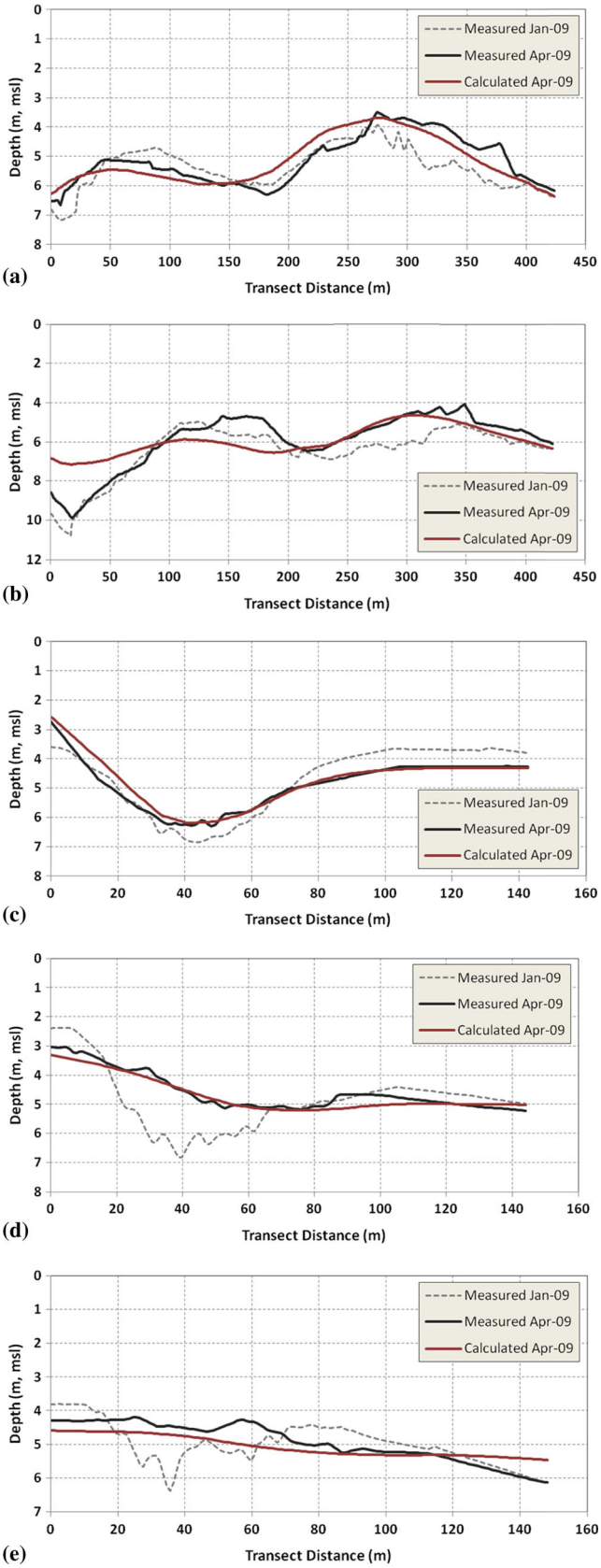

Fig. 19 Measured and calculated bed profiles at Shark River Inlet: **a** Transect 1, **b** Transect 2, **c** Transect 3, **d** Transect 4, and **e** Transect 5

jettied part of the channel and captured a small amount of shoaling and some deflation of the northern nearshore area adjacent to the north jetty. Transect 4 best illustrated the model comparison to the measured channel infilling at the location of greatest change. Transect 5 also had a good agreement demonstrating the model's capability to reproduce natural sedimentation morphology over the dredged channel.

8 Conclusions

This paper presents a depth-averaged 2-D model of unsteady flow, nonuniform sediment transport, and bed morphological changes under actions of current and waves. It solves the phase-averaged 2-D shallow water equations with wave radiation stresses and considers the general diffusion or mixing induced by current, waves, and wave breaking. The flow model is coupled with a spectral wave transformation model that solves the wave-action balance equation to determine the wave characteristics. The model computes the nonequilibrium transport of multiple-sized sediments, accounting for sediment entrainment induced by current and waves, the lag of sediment transport relative to the flow, the effect of bed slope on bedload transport, and the hiding and exposure mechanism in the nonuniform bed material. The model combines bed load and suspended load as total load and thus reduces the number of partial differential equations to be solved. This is particularly efficient when multiple-sized sediment transport is simulated. The model specifies the cross-shore boundary conditions by assuming well-developed longshore current and wave setup that are determined using the reduced 1-D momentum equations.

The model solves the flow and sediment transport equations using an implicit finite volume method based on a variety of meshes, such as nonuniform rectangular, telescoping (quadtree) rectangular, and hybrid triangular/quadrilateral meshes. The telescoping technology locally refines the mesh around structures of interest or where the topography and/or flow properties change rapidly, while the hybrid triangular/quadrilateral meshes can conveniently conform to irregular domains. The model adopts an unstructured index system to number the grid nodes for more flexibility of mesh generation and to incorporate all the meshes in a single model framework. The model uses the SIMPLEC algorithm with Rhie and Chow's (1983) momentum interpolation to handle the coupling of water level and velocity on a non-staggered grid. The sediment calculation is decoupled from the flow calculation, but the three components of the sediment module—nonuniform sediment transport, bed change, and bed material sorting equations—are solved in a coupled form. Thus, the flow and sediment transport model is quite stable and the computational time step for flow and sediment calculations is relatively long (up to the order of magnitude of 10 min).

The model has been tested extensively in many laboratory and field cases. Presented in this paper are three real-life cases, showing good performance of the model in predicting tidal flow with wave effects in an estuary, morphological evolution in a beach adjacent to a tidal inlet, and channel infilling at a tidal inlet. The model results are in generally good agreement with the measured data.

Acknowledgments This study is supported by the Coastal Inlets Research Program (CIRP), ERDC, U.S, Army Corps of Engineers, Vicksburg, MS, USA. Dr. Julie D. Rosati, Dr. Honghai Li, Mr. Mitchell Brown, Dr. Lihwa Lin, and Dr. Zeki Demirbilek are acknowledged for their collaborations and contributions.

The present paper reports a part of the latest developments and applications of the CMS2D model, which is managed by CIRP. More details on CMS2D can be found on CIRP's website: http://cirp.usace.army.mil.

References

Andrews DG, McIntyre ME (1978) An exact theory of nonlinear waves on Lagrangian mean flow. J Fluid Mech 89:609–646

Battjes JA (1972) Set-up due to irregular waves. Proc. 13th International Conference on Coastal Engineering, ASCE, 1993–2004

Battjes JA (1975) Modeling of turbulence in the surf zone. Proc. Symp. Model Techniques, San Francisco, USA, pp. 1050–1061

Battjes JA, Janssen J (1978) Energy loss and set-up due to breaking of random waves. Proc. 16th International Conference Coastal Engineering, ASCE, pp. 569–587

Bosboom J, Aarninkhof SGJ, Reniers AJHM, Roelvink JA, Walstra DJR (1997) UNIBEST-TC 2.0: overview of model formulations. Report H2305.42, Delft Hydraulics, The Netherlands

Bottom DL, Simenstad CA, Burke J, Baptista AM, Jay DA, Jones KK, Casillas E, Schiewe MH (2005) Salmon at river's end: the role of the estuary in the decline and recovery of Columbia River salmon. NOAA Technical Memorandum. NMFS-NWFSC-68, U.S. Department of Commerce

Buttolph AM, Reed CW, Kraus NC, Ono N, Larson M, Camenen B, Hanson H, Wamsley T, Zundel AK (2006) Two-dimensional depth-averaged circulation model CMS-M2D: Version 3.0, Report 2: Sediment transport and morphology change. Technical Report ERDC/CHL TR-06-9, Coastal and Hydraulics Laboratory, ERDC, US Army Corps of Engineers, Vicksburg, MS, USA

Camenen B, Larson M (2007) A unified sediment transport formulation for coastal inlet application. Technical Report ERDC-CHL CR-07-01, Coastal and Hydraulics Laboratory, ERDC, US Army Corps of Engineers, Vicksburg, MS, USA

Cayocca F (2001) Long-term morphological modeling of a tidal inlet: the Arcachon Basin, France. Coast Eng 42:115–142

Chawla A, Kirby JT (2002) Monochromatic and random wave breaking at blocking points. J Geophys Res 107(C7). doi:10.1029/2001JC001042

Chesher TJ, Wallace HM, Meadowcroft IC, Southgate HN (1993) PISCES, a morphodynamic coastal area model, First annual report. Report SR 337, HR Wallingford, UK

De Vriend HJ, Stive MJF (1987) Quasi-3D modeling of nearshore currents. Coast Eng 11:565–601

Dean RG, Dalrymple RA (1991) Water wave mechanics for engineers and scientist. World Scientific Publishing, p 353

Elias EPL, Gelfenbaum G, Van der Westhuysen AJ (2012) Validation of a coupled wave-flow model in a high energy setting: the mouth of the Columbia River. J Geophys Res 117:1–21

Exner FM (1925) Über die wechselwirkung zwischen wasser und geschiebe in flüssen. Akad Wiss Wien Math Naturwiss Klasse 134(2a):165–204

Fortunato AB, Olveira A (2004) A modeling system for tidally driven long-term morphodynamics. J Hydraul Res 42(4):626–634. doi:10.1080/00221686.2004.9728408

Han Q (1980) A study on the non-equilibrium transportation of suspended load. Proc. First International Symposium on River Sedimentation, Beijing, China

Hanson H, Kraus NC (1989) GENESIS: generalized model for simulating shoreline change, Report 1: technical reference. Technical Report CERC-89-19, U.S. Army Engineer Waterways Experiment Station, Coastal Engineering Research Center, Vicksburg, MS, USA

Hedegaard IB, Deigaard R (1988) A model for cross-shore sediment transport and coastal profile development. Proc. IAHR 2nd International Symposium on Wave Research and Coastal Engineering, Hannover, Germany

Holland KT, Elmore PA (2008) A review of heterogeneous sediments in coastal environments. Earth Sci Rev 89:116–134

Hsu SA (1988) Coastal meteorology. Academic Press, San Diego, California

Johnson HK, Zyserman JA (2002) Controlling spatial oscillations in bed level update schemes. Coast Eng 46(2):109–126

Johnson BD, Kobayashi N, Gravens MB (2012) Cross-shore numerical model CSHORE for waves, currents, sediment transport, and beach profile evolution. Technical Report ERDC/CHL TR-12-22, U.S. Army Engineer Research and Development Center, Coastal and Hydraulics Laboratory, Vicksburg, MS, USA

Jonsson IG (1990) Wave-current interactions. Chapter 7, The Sea. In: Le Mehaute B, Hanes D (eds). John Wiley and Sons, NY, p 65–120

Karambas TV (2003) Nonlinear wave modeling and sediment transport in the surf and swash zone. Advances in coastal modeling, V.C. Lakhan (ed.), Elsevier Oceanography Series, 67, Amsterdam, The Netherlands, 267–298

Karim MF, Kennedy JF (1982) IALLUVIAL: a computer-based flow- and sediment-routing for alluvial stream and its application to the Missouri River. Report No. 250, Iowa Institute of Hydraulic Research, University of Iowa, USA

Kraus NC, Larson M (1991) NMLONG—Numerical model for simulating the longshore current, Report 1: Model development and tests. Technical Report DRP-91-1, U.S. Army Engineer Waterways Experiment Station, Vicksburg, MS, USA

Kubatko EJ, Westerlink JJ, Dawson C (2006) An unstructured grid morphodynamic model with a discontinuous Galerkin method for bed evolution. Ocean Model 15(1–2):71–89

Landerman L, Sherwood CR, Gelfenbaum G, Lacy J, Ruggiero P, Wilson D, Chrisholm T, Kurrus K (2004) Grays Harbor sediment transport experiment: Spring 2001—data report. U.S. Geological Survey Data Series, USA

Larson M, Kraus NC (1989) SBEACH: Numerical model for simulating storm-induced beach change. Technical Report CERC-89-9, Waterways Experiment Station, Coastal Engineering Research Center, Vicksburg, MS, USA

Larson M, Hanson H, Kraus NC (2003) Numerical modeling of beach topography change. Advances in coastal modeling. In: Lakhan VC (ed), Elsevier Oceanography Series, 67, Amsterdam, The Netherlands, 337–365

Larson M, Westergren S, Hanson H (2015) Modeling beach profile response to varying waves and water levels with special focus on the subaerial region. Proc. 2015 International Conference on Coastal Sediments, World Scientific

Lesser G, Roelvink J, van Kester J, Stelling G (2004) Development and validation of a three-dimensional morphological model. Coast Eng 51(8–9):883–915

Lin L, Demirbilek Z, Mase H, Zheng J, Yamada F (2008) CMS-Wave: a nearshore spectral wave processes model for coastal inlets and navigation projects. Technical Report ERDC/CHL TR-08-13, Coastal and Hydraulics Laboratory, ERDC, US Army Corps of Engineers, Vicksburg, MS, USA

Lu YJ, Zuo LQ, Shao XJ (2005) A 2D mathematical model for sediment transport by waves and tidal currents. *China*. Ocean Eng 19(4):571–586

Mase H (2001) Multidirectional random wave transformation model based on energy balance equation. Coast Eng J 43(4):317–337

Mase H, Oki K, Hedges TS, Li HJ (2005) Extended energy-balance-equation wave model for multidirectional random wave transformation. Ocean Eng 32(8–9):961–985

Mason CC, Folk RL (1958) Differentiation of beach, dune and eolian flat environments by size analysis: Mustang Island, Texas. J Sediment Petrol 28(2):211–226

Mei CC (1989) The applied dynamics of ocean surface waves, Advanced Series on Ocean Engineering. World Scientific, New York

Miche M (1951) Le pouvoir reflechissant des ouvrages maritimes exposes a l'action de la houle. Annals des Ponts et Chau.ssess. 121e Annee: 285–319 (translated by Lincoln and Chevron, University of California, Berkeley, Wave Research Laboratory Series 3, Issue 363, June 1954).

Moritz HR (2005) Mouth of the Columbia River mega-transect instrument deployment. Internal document. U.S. Army Engineer District, Portland, Oregon

Nairn RB, Southgate HN (1993) Deterministic profile modelling of nearshore processes, part 2: sediment transport and beach profile development. Coast Eng 19(1–2):57–96

Pelnard-Considere R (1956) Essai de theorie de l'Evolution des forms de rivages en plage de sable et de galets, Fourth Journees de l'Hydrolique, les energies de la Mer, Question III, Rapport No. 1, 289–298

Phillips OM (1977) The dynamics of the upper ocean (2nd ed). Cambridge University Press

Phillips BC, Sutherland AJ (1989) Spatial lag effects in bed load sediment transport. J Hydraul Res 27(1):115–133

Powell MD, Vickery PJ, Reinhold TA (2003) Reduced drag coefficient for high wind speeds in tropical cyclones. Nature 422:279–283

Ranasinghe R, Pattiaratchi C, Masselink G (1999) A morphodynamic model to simulate the seasonal closure of tidal inlets. Coast Eng 37:1–36

Rhie TM, Chow A (1983) Numerical study of the turbulent flow past an isolated airfoil with trailing-edge separation. AIAA J 21:1525–1532

Rodi W (1993) Turbulence models and their applications in hydraulics, 3rd edn. IAHR Monograph, Rotterdam, The Netherlands

Roelvink JA, van Banning GKFM (1994) Design and development of Delft3D and application to coastal morphodynamics. *Hydrodynamics '94*, Verwey, Minns, Babovic & Maksimovic (eds), Balkema, Rotterdam, 451–455

Roelvink D, Reniers A, Dongeren AV, de Vries JVT, Lescinski J, McCall R (2010) XBeach model description and manual (version 6). UNESCO-IHE Institute for Water Education

Ruessink BG, Miles JR, Feddersen F, Guza RT, Elgar S (2001) Modeling the alongshore current on barred beaches. J Geophys Res 106(C10): 22451–22464

Sakai S, Kobayashi N, Koike K (1989) Wave breaking criterion with opposing current on sloping bottom: an extension of Goda's breaker index. Ann J Coast Eng JSCE 36:56–59 in Japanese

Sanchez A (2013) An implicit finite-volume depth-integrated model for coastal hydrodynamics and multiple-sized sediment transport. PhD dissertation, The University of Mississippi, MS, USA

Sanchez A, Wu W (2011) A non-equilibrium sediment transport model for coastal inlets and navigation channels. Journal of Coastal Research, Special Issue 59, 39–48

Sánchez-Arcilla A, Collado F, Rodriguez A (1990). Another quasi-3D model for surf-zone flows. Proc. 22nd International Conference on Coast Eng, 316–329

Soulsby R (1997) Dynamics of marine sands. Thomas Telford Publications, London, UK

Spasojevic M, Holly FM Jr (1993) Three-dimensional numerical simulation of mobile-bed hydrodynamics. Technical Report No. 367, Iowa Institute of Hydraulic Research, The University of Iowa, USA

Stive MJF, de Vriend HJ (1994) Shear stresses and mean flow in shoaling and breaking waves. Proc. 24th International Conference on Coastal Engineering, Kobe, Japan, pp. 594–608

Struiksma N, Olewensen KW, Flokstra C, de Vriend HJ (1985) Bed deformation in curved alluvial channels. J Hydraul Res 23(1):57–79

Svendsen IA (2006) Introduction to nearshore hydrodynamics. World Scientific. 722 p

Svendsen IA, Haas K, Zhao Q (2002). Quasi-3D nearshore circulation model, SHORECIRC, version 2.0. Center for Applied Coastal Research, University of Delaware, USA.

Szmytkiewicz M, Biegowski J, Kaczmarek LM, Okrój T, Ostrowski R, Pruszak Z, Rózynsky G, Skaja M (2000) Coastline changes nearby harbour structures: comparative analysis of one-line models versus field data. Coast Eng 40:199–139

Tajima Y, Madsen OS (2006) Modeling near-shore waves, surface rollers, and undertow velocity profiles. Journal of Waterway, Port and Coastal Ocean Eng 132:429–438

Van der Salm GLS (2013) Coastline modelling with UNIBEST: areas close to structures. M.S. thesis, Delft University of Technology, The Netherlands

Van Doormal JP, Raithby GD (1984) Enhancements of the SIMPLE method for predicting incompressible fluid flows. Num Heat Transfer 7:147–163

Van Rijn LC (1984a) Sediment transport, Part I: bed load transport. Journal of Hydraulic Engineering, ASCE, 110(10):1431–1456

Van Rijn LC (1984b) Sediment transport, Part II: suspended load transport. Journal of Hydraulic Engineering, ASCE, 110(11):1613–1641

Van Rijn LC (1989) Handbook of sediment transport by currents and waves. Technical Report H461, The Hague: Delft Hydraulics Laboratory

Van Rijn LC (2007a) Unified view of sediment transport by currents and waves, I: initiation of bed motion, bed roughness, and bed-load transport. Journal of Hydraulic Engineering, ASCE, 133(6):649–667

Van Rijn LC (2007b) Unified view of sediment transport by currents and waves, II: suspended transport. Journal of Hydraulic Engineering, ASCE, 133(6):668–689

Walstra DJR, Roelvink JA, Groeneweg J (2000) Calculation of wave-driven currents in a 3D mean flow model. 27th International Conference on Coastal Engineering, Sydney, 1050–1063

Wang P, Davis RA, Kraus NC (1998) Cross-shore distribution of sediment texture under breaking waves along low-wave-energy coasts. J Sediment Res 68(3):497–506

Warner JC, Sherwood CR, Signell RP, Harris K, Arango HG (2008) Development of a three-dimensional, regional, coupled wave, current, and sediment-transport model. Comput Geosci 34: 1284–1306

Watanabe A (1985) Three-dimensional predictive model of beach evolution around a structure. Proc. International Symposium of Water Wave Research, University of Hannover, Germany, 121–142

Watanabe A (1987) 3-dimensional numerical model of beach evolution. Proc. Coastal Sediments '87, N.C. Kraus (ed.), ASCE, Reston, VA, 802–817

Wu W (2004) Depth-averaged 2-D numerical modeling of unsteady flow and nonuniform sediment transport in open channels. Journal of Hydraulic Engineering, ASCE, 135(10): 1013–1024

Wu W (2007) Computational river dynamics. Taylor & Francis, London, 494p

Wu W, Lin Q (2015) A 3-D implicit finite-volume model of shallow water flows. Adv Water Resour 83(2015):263–276. doi:10.1016/ j.advwatres.2015.06.008

Wu W, Wang SSY, Jia Y (2000) Nonuniform sediment transport in alluvial rivers. J Hydraul Res 38(6):27–434

Wu W, Sanchez A, Zhang M (2011) An implicit 2-D shallow water flow model on unstructured quadtree rectangular mesh. Journal of Coastal Research, Special Issue, No. 59, pp. 15–26

Zhang H-M, Reynolds RW, Bates JJ (2006) Blended and gridded high resolution global sea surface wind speed and climatology from multiple satellites: 1987–present. American Meteorological Society 2006 Annual Meeting, Paper #P2.23, Atlanta, GA, USA

Zhu J (1991) A low-diffusive and oscillation-free convection scheme. Communications in Applied Numerical Methods 7:225–232